Polarization Dependent Photocurrents in Thin Films of the Topological Insulator Bi_2Se_3

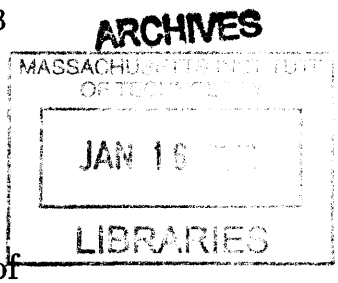

by

Claudia Lau

Submitted to the Department of Physics
in partial fulfillment of the requirements for the degree of

Bachelor of Science in Physics

at the

MASSACHUSETTS INSTITUTE OF TECHNOLOGY

June 2012

Author .....
Department of Physics
May 11, 2012

Certified by .....
Nuh Gedik
Associate Professor, Department of Physics
Thesis Supervisor

Accepted by .....
Nergis Mavalvala
Senior Thesis Coordinator, Department of Physics

Polarization Dependent Photocurrents in Thin Films of the Topological Insulator Bi_2Se_3

by

Claudia Lau

Submitted to the Department of Physics
on May 11, 2012, in partial fulfillment of the
requirements for the degree of
Bachelor of Science in Physics

Abstract

Topological insulators are a new class of three-dimensional quantum materials whose interior or bulk is an insulator but whose surface is a conductor. Bi_2Se_3 is a prototypical topological insulator that physicists at MIT are manufacturing and studying. Various interesting properties of the topological insulator include the flow of pure spin currents and topological protection.

Pure spin current, distinct from electric current, is a net flow of spin without a net flow of charge. Recent research at MIT has revealed that shining circularly polarized laser light on a topological insulator turns its surface's pure spin current into a spin-polarized electrical current. The band structure of the bulk of a topological insulator resembles that of an ordinary insulator; the conduction band and valence band are separated, with the Fermi level falling between them. However, for Bi_2Se_3, the conducting surface's dispersion relation can be modeled by a Dirac cone, which crosses the Fermi level. Electrons with opposing spins reside on opposite sides of the Dirac cone. Illuminating a topological insulator with either left or right circularly polarized light depopulates one side of the Dirac cone, leaving on the other side the desired spin-polarized electrical current.

In the experiment performed for this thesis, thin films of Bi_2Se_3 were grown on substrates of sapphire via molecular beam epitaxy (MBE). Electrical devices on a micron scale were then fabricated on the thin film surface and used to measure surface currents. Steps of this experiment included characterizing the surface quality of a sapphire substrate using atomic force microscopy (AFM), making electrical devices with Bi_2Se_3 via the processes of optical lithography, ion milling, and electron beam metal deposition. Photocurrents across these electrical devices were induced by the manipulation of optics and lasers and measured using low noise electronics.

Experimental results revealed that it was indeed possible to induce spin-polarized electrical currents on thin films of MBE grown Bi_2Se_3. The desired photocurrent was observed when the laser beam spot size was enlargened to illuminate the entirety of the Bi_2Se_3 device simultaneously. These results were not replicable when the laser was more tightly focused onto a smaller area. Scanning the focused laser beam across the

Bi_2Se_3 confirmed that different photocurrents were being induced at different points; these results led us to the conclude that there was something inhomogenous about our device. The reason behind this device inhomogeneity is still under investigation.

Thesis Supervisor: Nuh Gedik
Title: Associate Professor, Department of Physics

Acknowledgments

I would like to acknowledge James McIver for guiding me in the performance of this experiment and the writing of this thesis; Steve Drapcho for carrying out the experiments with me; Nuh Gedik for serving as my thesis supervisor; and Valla Fatemi, Lucas Orona, Hadar Steinberg, Pablo Jarillo-Herrero, Kurt Broderick, and Ferhat Katmis for their assistance in the fabrication of the devices and material synthesis.

Contents

List of Figures

Chapter 1

Introduction

The topological insulator is a new electronic phase of matter which is characterized by an insulating bulk but a conducting surface. The conducting surface states are of particular interest because of the distinctive way in which electrons behave on them. On the surface of a topological insulator, electrons arrange themselves into spin up electrons traveling in one direction and spin down electrons traveling in the opposite direction. This spin current has exciting potential applications in the area of spintronics (electronic devices based on electron spin). [18]

1.1 Overview of Sections

The scope of this thesis is to describe an experiment in which photocurrents were measured across the topological insulator Bi_2Se_3. Electronic devices were fabricated on thin films of Bi_2Se_3 grown on sapphire substrates. Photocurrents were then induced on the Bi_2Se_3 surface by laser light. Analysis of these photocurrents shed light on the nature of surface photocurrents of the topological insulator.

Background on the topological insulator and photocurrents are given in Chapters 1 and 2, respectively. Chapter 3 describes the design of the electronic devices used in this experiment and their fabrication process. The layout of the experiment and the experimental procedure is presented in Chapter 4. Chapter 5 details the experimental results, and conclusions are drawn in Chapter 6.

1.2 Topological Insulator Background

In the Landau classification system, phases of matters are characterized in terms of underlying broken symmetries. For example, crystals break continuous translational and rotational symmetry; magnets break time-reversal symmetry.[19] In the 1980s, the discovery of the a new phase of matter, the quantum Hall state, introduced a new classification system based on topological order. The topological insulator, discovered around 2006, is likewise characterized by topological order.

1.2.1 Topological Order

The name topological order is derived from the mathematical field of topology. Topology is the study of the properties of an object which are preserved under continuous deformation. The classic example in topology is the doughnut and the coffee cup. Imagining that these two objects were made of clay, the doughnut can be continuously deformed into the coffee cup and vice versa. Continuous deformations include stretching the object but no tearing or gluing. The underlying reason why the continuous deformation is possible is that both the coffee cup and doughnut possess a single hole.

The topological equivalence of the two objects is mathematically expressed in the Gauss-Bonnet Theorem. The Gauss-Bonnet Theorem states that for any closed surface, the surface integral

$$\int \kappa dA = 2\pi(2 - 2g) \tag{1.1}$$

where κ is the curvature and g is the number of holes in the object (see Figure 1-1 for an illustration). For both the doughnut and the coffee cup, $g = 1$ and $\int \kappa dA = 0$. These two seemingly distinct objects are actually topologically equivalent because they share the same values of g and $\int \kappa dA$, which are topological invariants.

Both the quantum Hall state and the topological insulator are likewise characterized in terms of their topological invariants. For the quantum Hall state, the

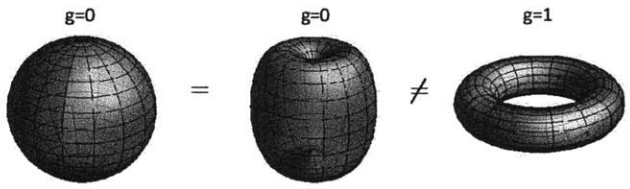

Figure 1-1: Illustration of the Gauss-Bonnet Theorem. Both the sphere on the left and the central deformed sphere have $g = 1$ and $\int \kappa dA = 4\pi$. They are topologically equivalent and distinct from the doughnut which has $g = 1$ and $\int \kappa dA = 0$. Image courtesy of James McIver.

topological invariant is called the Chern number and is related to the Berry flux and the Hall conductivity. For the topological insulator, the invariant (called the Z_2 invariant) is more complicated, but it is essential to note that it is determined by the material's bulk (*not* the surface.) In both cases, the topological invariant is unchanged by continuous (or adiabatic) tuning of the Hamiltonian. Only a drastic "tear," such as the closing of an energy gap in the band structure, can change the invariant. The energy gap is analogous to the hole g in Equation 1.1.

With this understanding of topological invariance, we see that within topological classification, the insulator and semiconductor are equivalent. These two phases of matter are only distinguished through the difference in the magnitude of their energy gaps, where $E_{gap,insulator} \gg E_{gap,semiconductor}$. Continuously increasing or decreasing the energy gap transforms one state into the other. During this transition, the energy gap never closes, so the topological invariant never changes.[10]

1.2.2 Quantum Hall State

Not all electronic states with an energy gap are equivalent, a counterexample being the quantum Hall state, a close "cousin" of the 2-dimensional topological insulator.[10] Discovered in the 1980s, the quantum Hall state is the simplest topologically ordered state. Its topological order, which is manifested by the quantized Hall conductivity, distinguishes it from a traditional insulator.[14]

The quantum Hall state is a result of the integer quantum Hall effect, a phe-

nomenon that occurs when electrons are confined to a 2-dimensional interface in a strong magnetic field. The magnetic field, oriented normal to the 2D surface, causes the electrons to feel a Lorentz force, $\vec{F} = e\vec{v} \times \vec{B}$, where e is the electron charge, $\vec{v}$ is the electron's velocity, and $\vec{B}$ is the magnetic field. As the Lorentz force $\vec{F}$ is directed along the 2D surface and perpendicular to the electron velocity $\vec{v}$, the electrons on the 2D surface experience centripetal acceleration, moving them in circular orbits. This circular motion is consistent with classical mechanics; however, since electrons are quantized, quantum mechanics must be considered. In the quantum mechanical picture, these circular orbits are quantized orbitals. The electrons move with a quantized cyclotron frequency ω_c.

Because of this orbital quantization, the electrons arrange themselves into Landau levels; these levels are separated by energy $E = \hbar\omega_c$. Here, $\hbar = h/2\pi$, where h is Planck's constant; and the cyclotron frequency $\omega_c = \frac{eB}{mc}$, where e is the electron charge, B is the magnitude of the magnetic field, m is the electron mass, and c is the speed of light. The structure of these Landau levels is very similar to the band structure of an insulator. The quantized energy $E = \hbar\omega_c$ forms an energy gap between the Landau levels, just as an energy gap separates a insulator's conduction band from its valence band. [10]

Although the quantum Hall state is thus a gapped band structure, it remains topologically distinct from an insulator. The distinction lies in the Chern number, discovered in 1982 by Thouless, Kohmoto, Nightingale, and den Nijs (TKNN). For a single band, the Chern number is equal to the total Berry flux in the Brillouin zone:

$$n_m = \frac{1}{2\pi}\int(\nabla \times A_m)d^2\vec{k} \tag{1.2}$$

where $A_m = i\langle u_m|\nabla_k|u_m\rangle$ and $|u_m(\vec{k})\rangle$ is the Bloch wave function. The Block wave function describes an electron in a periodic potential. (Solids generally have periodic potentials due to their regular arrangement of atoms.) The Brillouin zone is a single "cell" of the periodic potential. The Bloch wave function in the Brillouin zone is replicated identically in all the other cells because of the periodicity. In an occupied

band m, the the Bloch wave function $|u_m(\vec{k})\rangle$ acquires a Berry's phase while traversing the Brillouin zone. The Berry's phase is given by the line integral around a closed loop in parameter-space: $\oint A_m dk$. As a geometric phase, the Berry's phase depends only on the path taken by the electron and *not* on the elapsed time. Applying Stoke's theorem to the line integral $\oint A_m dk$ yields the Berry flux in Equation 1.2. [9] The total Berry flux gives the Chern number.

The total Chern number is the sum of the Chern number over all N occupied bands: $n = \sum_{m=1}^{N} n_m$.[10] For an insulator $n = 0$, and for the quantum Hall state n is a positive integer.

The Chern number is insensitive to small changes of band structure or smooth changes in material parameters. Since the invariant is integer quantized, it cannot change when the Hamiltonian varies smoothly. The invariant only changes at a phase transition where the energy gap vanishes. [14] [10] Using topological classification, phases of matter with different Chern numbers are distinct phases.

The quantized Hall conductivity, which occurs for currents in the quantum Hall state but not the Hall insulator, is dependent upon the Chern number. In the quantum Hall state, when an electric field $\vec{E}$ is present, oriented parallel to the 2D surface described above, the cyclotron orbits experince a force $\vec{F} = e\vec{E}$. The orbits then drift along the surface, creating a Hall current. A Hall current is characterized by the Hall conductivity $\sigma = \frac{I}{V}$, where I is the current and V is the voltage perpendicular to it. For the quantum Hall state, the Hall conductivity is quantized in units of fundamental constants: $\sigma = n\frac{e^2}{h}$, where n is the Chern invariant, e is the electron charge, and h is Planck's constant. [10] As $n = 0$ for an insulator, the quantized Hall current is a phenomenon unique to the quantum Hall state.

The Chern number n is also equal to the number of edge states of a system. [20] An edge state is illustrated in Figure 1-2. As the quantum Hall state exists on a 2D surface, at the 1D boundary the quantized orbitals are broken. The orbitals "bounce" off the edge in the manner seen in Figure 1-2. The $\vec{k}$-space figure in Figure 1-2 shows that there is no energy gap along the edge; the gapless edge states are therefore conducting. It is also significant to note that these edge states propagate in only one

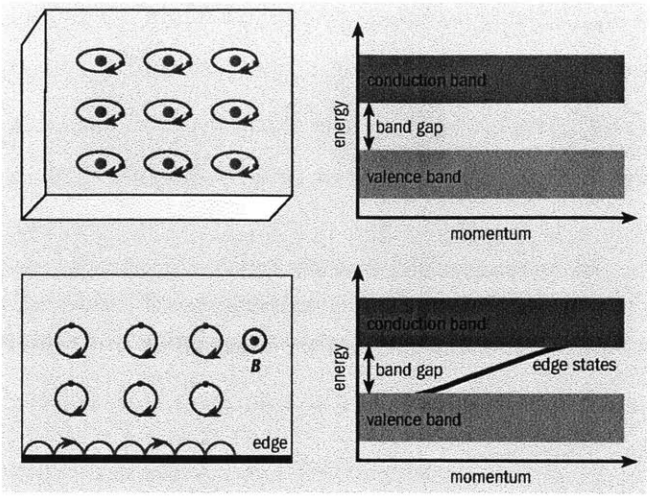

Figure 1-2: Comparison of an ordinary insulator (top) and a quantum Hall insulator (bottom). The 2 different phases of matter are seen in real space (left) and momentum space (right). The magnetic field B points out of the page. Image from [18]

direction. Since there are no backward moving modes, the electric current must necessarily propagate forwards. The edge states are topologically protected in that they are insensitive to disorder (impurities in the material) and cannot scatter backwards. Therefore, edge states have perfectly quantized electronic transport, where no energy is dissipated as heat. [18] Similar dissipationless edge states are likewise present in the topological insulator.

1.2.3 2D TI: Quantum Spin Hall Insulator

The quantum Hall state occurs only in the presence of an external magnetic field, which is needed to provide the Lorentz force and breaks time-reversal symmetry.[10] In contrast, for the topological insulator no external magnetic field is required. The topological insulator's dissipationless edge (or surface) states are protected by time reversal symmetry, and if magnetic impurites are introduced, this protection is lost.

In the toplogical insulator, spin-orbit coupling plays the role of the magnetic field, allowing for a topologically ordered system without the breaking of time-reversal symmetry. Spin-orbit coupling is the interaction between an electron's spin angular momentum $\vec{S}$ and its orbital angular momentum $\vec{L}$. It introduces an $\vec{L} \cdot \vec{S}$ term

into the system's Hamiltonian, which splits the band structure's energy levels. This energy is splitting is similar to the creation of Landau levels in the quantum Hall state. In atoms with high atomic number (such as bismuth), spin-orbit coupling is strong. [19] Its influence on the electrons resembles that of a magnetic field. Like a magnetic field, spin-orbit coupling provides a velocity-dependent force. The direction of the spin-orbit coupling "field" changes with the direction of the spin. [4] [18] [2]

The 2-dimensional topological insulator (or 2D TI) is called the quantum spin Hall insulator (QSHI). In the 2D TI, spin up and spin down electrons propagate in opposite directions on the edge. These edge states are protected by time-reversal symmetry. The Hall conductance of a the 2D TI is 0 due to cancelling between the spin up and spin down electrons.[18] Figure 1-3 explains the mechanism behind the 2D TI's edge states.

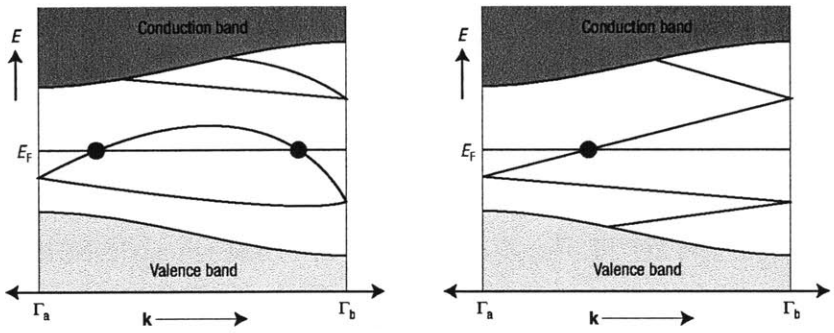

Figure 1-3: Left: Trivial insulator: between 2 Kramer's degenerate points (Γ_a and Γ_b), the edge states cross the Fermi energy E_F an even number of times. These edge states *can* be eliminated. Right: QSHI: between 2 Kramer's degenerate points (Γ_a and Γ_b), the edge states cross the Fermi energy E_F an odd number of times. These edge states *cannot* be eliminated; they are topologically protected. Image source [14].

The 2D TI has a 2-dimensional Brillouin zone, in which there exist 4 special momenta called Kramer's degenerate points. These points are labeled Γ_{1-4} and are also known as the time reversal invariant momenta (TRIM). According to Kramer's theorem, time-reversal symmetry requires that all states must come in degenerate pairs at any one of the TRIM.[14] [6] In other areas of the Brillouin zone, the states are *non*degenerate as they have been split by the spin-orbit coupling $\vec{L} \cdot \vec{S}$. [15]

The way in which edge states traverse between 2 TRIM, Γ_a and Γ_b determines

the value of the 2D TI's Z_2 topological invariant. Edge states are those states which traverse the bandgap of the solid. As seen in the Figure 1-3, the bandgap separates the occupied valence band from the unoccupied conduction band. The Fermi energy E_F lies within the bandgap. In the left hand diagram in Figure 1-3, the edge state crosses the Fermi energy twice. Such an edge state can be eliminated by "pushing" the state out of the gap. This is contrasted by the right hand diagram of Figure 1-3, in which the edge state crosses the Fermi energy once. This edge state, which connects the valence band to the conduction band, cannot be eliminated or pushed out of the gap; instead it is topologically protected. [11]

More generally, if the edge states cross the Fermi energy an even number of times between two TRIM, Γ_a and Γ_b, they are not topologically protected. The Z_2 topological invariant has the value $\nu = 0$, denoting that the material is a trivial insulator. If the edge states cross the Fermi energy an odd number of times between two TRIM, Γ_a and Γ_b, they are topologically protected. The Z_2 topological invariant has the value $\nu = 1$, denoting that the material is a 2D topological insulator. We see that unlike the quantum Hall state, in which the Chern invariant n could take the value of any positive integer, for the 2D TI, the Z_2 topological invariant is restricted to two values only: $\nu = 0$ or $\nu = 1$.

The underlying reason why an edge state will cross the Fermi energy a certain number of times is dependent upon the band strucutre. Depending on the occupied Bloch wave functions (the electronic states in the valence band), each TRIM Γ_a can be associated with a value of $\delta_a = \pm 1$. The value of ν is related to these δ_a by the following equation:

$$(-1)^{\nu} = \Pi_{a=1}^{4} \delta_a \tag{1.3}$$

This mathematical formulation can be extended to account for the topological invariants of the 3D topological insulator discussed in the next section.

The first experimentally observed 2D TI were (Hg,Cd)Te quantum wells, whose conducting edge states were measured in 2007. Quantum wells are artificial materials (i.e. they are fabricated in a laboratory and do not occur in nature). The

(Hg,Cd)Te quantum well consists of a thin layer of mercury telluride (HgTe) "sandwiched" between layers of cadmium telluride (CdTe). [18] Both HgTe and CdTe are semiconductors. CdTe, the barrier material, has the standard band progression where the s-type band lies above the p-type band. However, HgTe, the well material, has an inverted band progression where the p-type band lies above the s-type band.

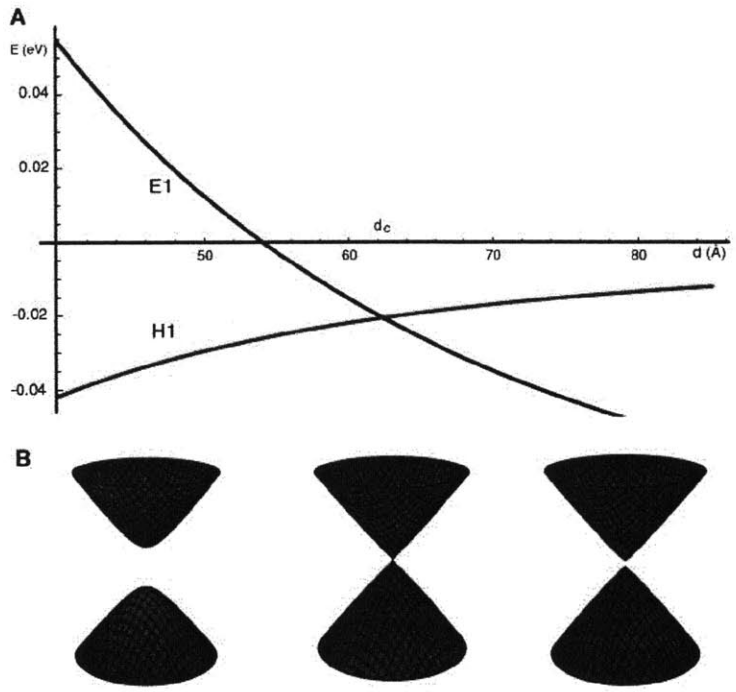

Figure 1-4: A) Energy of the upper and lower bands vs. quantum well thickness d. B) The band inversion that occurs as the Z_2 topological invariant changes. Left: $d > d_{critical}$ Center: $d = d_{critical}$ Right: $d < d_{critical}$ Image from [1]

In the (Hg,Cd)Te quantum well, when the HgTe layer is thin ($d < d_{critical} = 6.3$ nm), the CdTe band structure dominates so the s-type band lies above the p-type band. However, if the HgTe layer has thickness $d > d_{critical}$, then the 2D bands of the quantum well *invert*. [1] [10] This band inversion is illustrated in Figure 1-4. The band inversion which occurs at $d_{critical} = 6.3$ nm signifies a topological phase transition, where the topological invariant has changed from $\nu = 0$ to $\nu = 1$. At $d = d_{critical}$ the energy gap between the s-type band and the p-type band vanishes, and the system transitions between 2 topologically distinct phases of matter. This

transition is analogous to the topological phase transition depicted in Figure 1-1, where the hole g vanished, turning the doughtnut into a sphere.

1.2.4 3D TI

The quantum Hall state has no 3D analog, but the 2-dimensional topological insulator has a 3D analog in the 3-dimensional topological insulator. Unlike the 2D TI and the quantum Hall state, which are each characterized by 1 topological invariant, the 3D TI has 4 topological invariants. The 4 Z_2 topological invariants are written in the following form: $\nu_0; (\nu_1, \nu_2, \nu_3)$. Like in the case for the 2D TI, each topological invariant has only 2 possible values: $\nu_i = 0$ or $\nu_i = 1$. There are therefore 2^4, or 16, distinct classes of the 3D topological insulator. [6] The 3D Z_2 topological invariants can be mathematically expressed similarly to the 2D TI invariant (see the 2D TI invariant in Equation 1.3). The main difference is that in the 3D case, the Brillouin zone is 3-dimensional and there are 8 TRIM instead of 4 (see Figure 1-5).

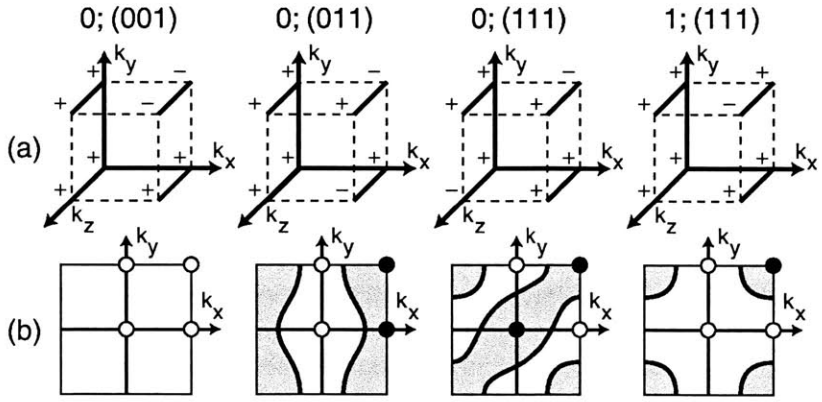

Figure 1-5: 4 possible 3D TI phases. a) The 3-dimensional Brillouin zone of the 3D TI has 8 TRIM. Each is associated with a value $\delta = \pm 1$. b) The projection of the 3D Brillouin zone onto the surface Brillouin zone. The 4 Dirac points are separated by Fermi arcs. Image source [6]

The Z_2 topological invariants can be expressed mathematically as follows:

$$(-1)^{\nu_0} = \Pi_{i=1}^{8} \delta_i \tag{1.4}$$

$$(-1)^{\nu_i=1,2,3} = \Pi_{n_{j\neq i}=0,1;n_i=1}\delta_{n_1 n_2 n_3} \tag{1.5}$$

Again the $\delta_{n_i} = \pm 1$ and is determined by Bloch wave functions in the bulk of the material. Figure 1-5 a) displays the 3D Brillouin zone for 4 different topological insulators. The 8 corners of the cube are the 8 TRIM (Γ_{1-8}). Each of these Γ points is labeled with a '+' or '-', corresponding to $\delta = +1$ and $\delta = -1$. Figure 1-5 b) shows the projection of the 8 TRIM onto the 2D surface Brillouin zone. If the 2 TRIM at the same k_x and k_y are of the same sign, the surface TRIM is denoted by an open circle. If the 2 TRIM are of different signs, the surface TRIM is denoted by a closed circle. The surface TRIM in Figure 1-5 b) are called Dirac points. Again, these points are subject to Kramer's degeneracy, as in the 2D version. [6] [5]

As seen in the 4 examples in Figure 1-5 b), an open circle Dirac point must be separated from a closed circle Dirac point by a surface state (called a surface Fermi state since it crosses the Fermi energy). Between two open circles or two closed circles, there is no separating surface state. We see therefore how the values of δ and therefore the topological invariants $\nu_0; (\nu_1, \nu_2, \nu_3)$ determine the number of surface crossings between the Dirac points. The surface state crossing is analogous to the 2D TI's edge state crossing (seen in Figure 1-3).

The most important of the 4 Z_2 topological invariants is ν_0, which determines whether the topological insulator is strong ($\nu_0 = 1$) or weak ($\nu_0 = 0$). The other topological invariants (ν_1, ν_2, ν_3) give information on the dispersion and topology of the Fermi surface states.

In the weak topological insulator ($\nu_0 = 0$), the surface Fermi arc encloses an even number of Dirac points. 3 examples of the weak topological insulator are shown in Figure 1-5. The surface states of the weak TI are not protected by time-reversal symmetry and can therefore be localized in the presence of disorder. [10] Therefore, while a perfectly clean weak TI is topologically distinct from the trivial insulator, with disorder this distinction is effectively eliminated.[6] The weak topological insulator can be constructed by stacking 2-dimensional TI's on top of each other.

In the strong topological insulator ($\nu_0 = 1$), the surface Fermi arc encloses an

odd number of Dirac points. The strong topological insulator shown in Figure 1-5 has one Dirac point enclosed by a surface Fermi arc. This creates a Dirac cone, like the one seen in Figure 1-6. The surface states of the strong TI are topologically protected so that they cannot be eliminated by disorder or by chemical passivation. The topological protection is due to the π Berry's phase which an electron acquires from traveling along the circular Fermi arc like the one seen in Figure 1-5. [6] Unlike the weak topological insulator, the strong topological insulator cannot be constructed by stacking the 2-dimensional topological insulator. Because of the dissipationless and topologically protected metallic surface states, the strong topological insulator is well suited for experimental study. [19] It is additionally helpful that the surface states come from properties in the bulk of the material and therefore have no dependence on how the material was cut. [18]

The first 3D TI discovered was the semiconducting alloy bismuth antimony Bi_xSb_{1-x}, whose surface bands were mapped via angle resolved photoemission spectroscopy (ARPES) in 2008.[13] The 2D topological insulator was studied initially with transport experiments. However, it is difficult to study the 3D topological insulator using transport experiments because of residual bulk conductivity. Ideally the topological insulator bulk is an insulator, but in practice there is residual conductivity from impurities. Currents in the bulk therefore tend to obscure the results of surface transport experiments. [18] ARPES, however, circumvents the problem of bulk conductivity and has yielded good experimental results for the 3D TI. [10] ARPES is a technique based on the photoelectric effect. In ARPES, photons are fired at a material sample, ejecting electrons from the material's surface. By analyzing the energy, momentum, and spin of the ejected electrons, the material's band structure can be determined. [18] ARPES experiments have successfully demonstrated that the surface states of the strong TI are nondegenerate and spin polarized. Additionally, they have also provided evidence for the π Berry's phase. [12]

Since the mapping of Bi_xSb_{1-x} in 2008, more 3D TI's have been discovered. Among these new discoveries are Bi_2Se_3 and Bi_2Te_3. Bi_2Se_3, Bi_2Te_3 and most other 3D topological insulators are fairly standard bulk semiconductors, whose topological

characteristics can survive to high temperatures. [18]

The topological insulator used in the experiments performed for this thesis was Bi_2Se_3. Bi_2Se_3 is a strong topological insulator; it has a band inversion at $\vec{k} = 0$ and belongs to the $1;(0,0,0)$ class. Bi_2Se_3 is better suited for experimental study than Bi_xSb_{1-x} was for several reasons. Firstly, Bi_2Se_3 has a larger band gap (0.3 eV) than Bi_xSb_{1-x}. It therefore exhibits TI behavior at not only low temperatures but also room temperature, making it easier to use for applications and experimentation. Bi_2Se_3 also has a simpler surface spectrum, an idealized single Dirac cone. Furthermore, since Bi_2Se_3 is a pure compound instead of an alloy, samples can be prepared at higher purity, which gives clearer experimental results in ARPES and for other experimental techniques. However residual bulk conductivity, which is due to impurity and self-doping states, remains a challenge in the experimental study of Bi_2Se_3.[10]

1.2.5 Motivations for Photocurrents in TI's

In the edge states of the 2D TI, spin up electrons travel along one direction and spin down electrons travel in the opposite direction. The behavior of electrons at these edge states suggests that the momentum and spin of the electron are "locked" with respect to each other. An electron with momentum $\vec{k}$ necessarily has spin up, while an electron of opposite momentum -$\vec{k}$ necessarily has spin down. On the planar metal surface of the 3D TI, the electron momentum is no longer restricted to 2 opposite directions. However, the electron spin and momentum are still "locked;" in this case the spin is locked perpendicular to momentum.[18] Ordinary metals are spin degenerate, having both spin up and spin down electrons at every point on the Fermi surface. The metallic boundary of a 3D strong TI is unique in that it is *not* spin degenerate.

Time-reversal symmetry requires that the surface states at $\vec{k}$ and $-\vec{k}$ have opposite spin. Therefore as the $\vec{k}$ vector rotates around a surface Fermi arc, like in Figure 1-6, the spin also rotates around the surface Fermi arc. Going around a Fermi circle, the spin rotates by 2π so the electron acquires a Berry's phase of π. [10] [6] More generally

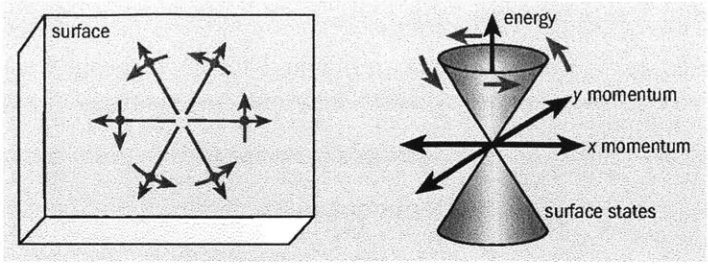

Figure 1-6: On the 2D metallic boundary of the 3D TI, the electron spin (red arrow) is locked perpendicular to its momentum (blue arrow). On the left, the electron travels in a circle in real space. In $\vec{k}$-space, the associated 2D energy-momentum relation is a Dirac cone structure. Image source [18].

a strong topological insulator (one whose Fermi arc encloses an odd number of Dirac points) necessarily has a π Berry's phase. This Berry's phase contributes to the topological protection of the dissipationless surface states. For most known materials and for the weak topological insulator, which do not have topological protection, the Berry's phase is 0. [12]

Because of momentum-spin locking, the currents which flow on the 2D metallic boundary of the 3D TI are pure spin currents. A pure spin current is a net flow of spin without a net flow of charge. Pure spin currents propagate in equilibrium; when optically driven out of equilibrium, the pure spin current is transformed into spin-polarized, net electric current. In the spin photoconductive effect, an external voltage bias is needed to obtain spin-polarized current. In contrast, for spin-polarized photocurrent, the irradiated sample serves as its own current source. [7] The spin-polarized photocurrent can be controlled by variation of the incident light polarization.

As pure spin current occurs naturally on the surface of the topological insulator, the topological insulator is well suited for experiments on spin-polarized photocurrent. TI spin-polarized photocurrent has exciting applications in probing the dynamics of topological insulators and for opto-spintronic devices. [16]

Chapter 2

Polarization Dependent Photocurrent Background

A photocurrent is an electric current that flows as the result of exposure to radiant power. The following equation relates a photocurrent j to the incident light (or radiation field $\vec{E}$):

$$j_\lambda = \sum_{\mu\nu} \chi_{\lambda\mu\nu} E_\nu E_\nu^* + \sum_{\delta\mu\nu} T_{\lambda\delta\mu\nu} E_\mu E_\nu^* \tag{2.1}$$

where $E_\nu^* = E_\nu^*(\omega) = E_\nu(-\omega)$ is the complex conjugate of $E_n u$. $\vec{E} = \vec{E}(\omega)$ is the electric field associated with the incident light, ω is the electric field frequency, and $\vec{q}$ is the electric field wave vector. The expansion coefficients $\chi_{\lambda\mu\nu}$ and $T_{\lambda\delta\mu\nu}$ are third and fourth rank tensors, respectively. The first term on the right hand side of Equation 2.1 represents the surface photocurrent from the photogalvanic effect. The second term on the right hand side represents the bulk photocurrent from the photon drag effect. [7]

In this thesis' experiment, polarization dependent photocurrent was excited and measured on the surface of the topological insulator Bi_2Se_3. However, photocurrent has also been observed and studied in many other materials. Sections 2.1 and 2.2 provide background on photocurrent gathered from studies in quantum wells.

2.1 Surface Photocurrent

The phenomenon responsible for the surface photocurrent, $j_\lambda = \sum_{\mu\nu} \chi_{\lambda\mu\nu} E_\nu E_\nu^*$, is the photogalvanic effect. The photogalvanic effect occurs when spin-polarized electrons are asymmetrically distributed in momentum space ($\vec{k}$-space). (Note: while in $\vec{k}$-space the electrons have been asymmetrically excited, in real space the electron distribution remains uniform.) The asymmetrical $\vec{k}$-space distribution is optically driven (*photo*) and leads to a net flow of current (*galvanic*). The net current flow satisfies the system's need to return to a symmetric $\vec{k}$-space distribution. There are two versions of the photogalvanic effect: the circular photogalvanic effect (CPGE) and the linear photogalvanic effect (LPGE). In the CPGE, circuarly polarized light drives the system into asymmetry, and in the LPGE, linearly polarized light drives the system into asymmetry.

Electrons can be optically driven into an asymmetric momentum distribution because their transitions are governed by certain selection rules. The standard selection rules governing electron transitions are given in Equation 2.2:

$$\begin{aligned} \Delta l &= \pm 1 \\ \Delta m_l &= 0, \pm 1 \\ \Delta m_s &= 0 \end{aligned} \tag{2.2}$$

where l is the azimuthal or orbital angular momentum quantum number, m_l is the magnetic quantum number, and m_s is the spin quantum number. The azimuthal quantum number l takes values $0 \leq l \leq n-1$, where n is the principal quantum number and must be a positive integer. The magnetic quantum number m_l takes values $-l \leq m_l \leq l$. The spin quantum number $m_s = \pm 1/2$ for an electron. [9]

In addition to the standard selection rules given in Equation 2.2, electron transitions are also governed by angular momentum conservation rules. Unlike the standard selection rules given in Equation 2.2, the angular momentum conservation rules are dependent on the polarization of incident light. These angular momentum conserva-

tion rules are given in Equation 2.3:

$$\Delta m_j = \begin{cases} 0 & \text{linearly polarized light} \\ +1 & \sigma^+ \text{ right circularly polarized light} \\ -1 & \sigma^- \text{ left circularly polarized light} \end{cases} \tag{2.3}$$

where $m_j = m_l + m_s$ and is called the total angular momentum quantum number.

The standard selection rules given in Equation 2.2 are bent (or changed) for systems subject to spin-orbit coupling. Spin-orbit coupling mixes quantum numbers m_l and m_s, leading to different electron transition probabilities. In systems with spin-orbit coupling, spin degeneracy is lifted by $\vec{k}$-linear terms in the Hamiltonian. The spin-dependent $\vec{k}$-linear terms lead to a splitting of electronic subbands in $\vec{k}$-space. A single band which was formerly spin degenerate is divided into 2 subbands; one with only spin up electrons and the other with only spin down electrons.

Unlike the standard selection rules, the angular momentum conservation rules in Equation 2.3 are not changed by spin-orbit coupling. In a system with lifted spin degeneracy, the optical transitions retain the standard polarization sensitivity. The combination of lifted spin degeneracy and polarization dependent optical transitions creates the asymmetric momentum distribution driving the photogalvanic effect. Since bulk bands are necessarily spin degenerate, we note that the photogalvanic effect can only occur on a material's surface. The photogalvanic effect creates only surface photocurrents.

In Equation 2.1, the surface photocurrent was expressed by the term $j_\lambda = \sum_{\mu\nu} \chi_{\lambda\mu\nu} E_\nu E_\nu^*$. Via mathematical manipulation this can be rewritten as a sum of 2 separate components:

$$\begin{aligned} j_\lambda &= \sum_{\mu\nu} \chi_{\lambda\mu\nu} E_\nu E_\nu^* \\ &= \sum_{\mu\nu} \chi_{\lambda\mu\nu} \{E_\mu E_\nu^*\} + \sum_{\rho} \gamma_{\lambda\rho} i(E \times E*)_\rho \end{aligned} \tag{2.4}$$

where the first term on the right hand side represents the contribution from the linear photogalvanic effect and the second term represents the contribution from the circular photogalvanic effect. These two effects are discussed in greater detail in Sections 2.1.1 and 2.1.2.

2.1.1 Circular Photogalvanic Effect

In the circular photogalvanic effect (CPGE), incident circularly polarized light creates an asymmetrical distribution of electrons in $\vec{k}$-space. In the microscopic picture of this phenomenon, angular momentum from the incident photons is transferred into the directed motion of electrons. This transfer of angular momentum into a directed motion is the electrical analog of the way in which the rotating wheel of a car moves a car forward.

In Equation 2.4, the CPGE photocurrent can be rewritten as $i(E \times E*)_\rho = \hat{e}P_{circ}E^2$, where $\hat{e} = \vec{q}/q$ is the unit vector pointing in the direction of the light propagation and P_{circ} is the degree of the light circular polarization (the radiation helicity). In this formulation, we see that the CPGE photocurrent is proportional to the square of the radiation field: $j_y \propto E^2$, [7] [17] and therefore proportional to the radiation power. The photocurrent is also proportional to the radiation helicity P_{circ}, where $P_{circ} = -1$ for left circularly polarized light and $P_{circ} = +1$ for right circularly polarized light.

The helicity dependence of the CPGE photocurrent can be observed experimentally by reversing the helicity of the radiation. When the the radiation field changes from σ^+ (right circularly polarized light) to σ^- (left circularly polarized light), the CPGE photocurrent reverses its direction because the "center of mass" of the optical transitions has shifted.[7]. The CPGE photocurrent is unique in this respect since none of the other photocurrents represented in Equation 2.1 share this helicity dependence.

Figure 2-1 shows how optical transitions due to circularly polarized light lead to a spin photocurrent in a quantum well. In Figure 2-1, the system is excited by right circularly polarized light σ^+. Depending on the incoming photon energy, this optical

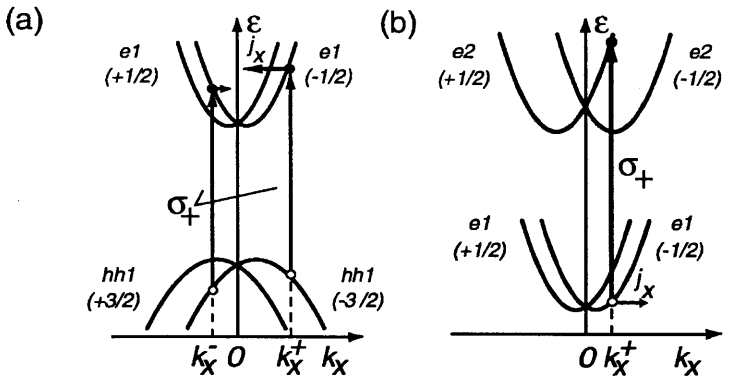

Figure 2-1: Microscopic picture of the circular photogalvanic effect for a) electron transitions between the valence (hh1) and conduction (e1) band and b) electron transitions between subbands e1 and e2 of the conduction band. Image source [8]

excitation leads to electron transitions between the valence band and the conduction band (Figure 2-1 a)) or electron transitions between subbands of the conduction (Figure 2-1 b)). In both cases the splitting of the bands into subbands is crucial to the asymmetrical excitation and the generation of photocurrent. As seen in Figure 2-1, both the conduction and valence band have lifted spin degeneracy. Spin up electrons reside on the left hand subbands ($k_x < 0$), and spin down electrons reside on the right hand subbands ($k_x > 0$).

By the optical selection rules given in Equation 2.3, electrons excited by right circularly polarized light σ^+ must make a transition such that that $\Delta m_j = +1$. In Figure 2-1 a), electrons transition from the valence heavy hole subband hh1 with $m_j = -3/2$ to the conduction subband e1 with $m_j = -1/2$. Because of the way in which the bands have been split by spin-orbit coupling, the "center of mass" of these transitions occurs not at $k_x = 0$, but instead at k_x^+. Electrons gather at k_x^+ in the conduction band. To counter this imbalance of electrons (i.e. the *asymmetrical* distribution in $\vec{k}$-space), a photocurrent j_x carries the e1 electrons back towards $k_x = 0$. Figure 2-1 b) shows a similar process. Electrons transition from conduction subband e1 with $m_j = -1/2$ to the conduction subband e2 with $m_j = +1/2$. These transitions create a dearth of electrons at k_x^+ on e1. Again, a photocurrent j_x settles this imbalance. [8] These photocurrents j_x are all spin-polarized because they occur in electronic

subbands of nondegenerate spin.

2.1.2 Linear Photogalvanic Effect

The second contributor to the surface photocurrent is the linear photogalvanic effect. The microscopic picture of the LPGE is not as well-understood as the picture for the circular photogalvanic effect.[16] However, it is known that the LPGE is caused by asymmetry in $\vec{k}$-space of excited electrons and the effect is dependent upon momentum relaxation due to scattering of the free electrons. The scattering, which occurs off phonons, static defects, and other electrons, contributes signficantly to the asymmetry of the system.[7] Unlike the CPGE, the LPGE photocurrent is helicity-independent, as it depends not on circularly polarized light but on linearly polarized light. If the incident light reverses its direction of propagation, the LPGE photocurrent also reverses its direction. [8] [17]

The linear photogalvanic effect was first observed in the 1950s and has been extensively studied in bulk materials such as GaAs. The effect has already been successfully applied as a fast detector for the degree of linear polarization. Physicists are now attempting to apply the circular photogalvanic effect as a fast detector for the degree of circular polarization.

2.2 Bulk Photocurrent: Photon Drag Effect

The bulk photocurrent is due to the photon drag effect, a phenomenon that involves the the transfer of linear momentum from incident photons to excited electrons as a means of generating electric current.[16] Like the linear photogalvanic effect, the photon drag effect depends on linearly polarized light and is therefore helicity-independent. If the incident light reverses its direction of propagation, the photon drag photocurrent also reverses its direction. Unlike the photogalvanic effect, however, the photon drag effect does not require an asymmetric distribution in $\vec{k}$-space. It also does not require lifted spin degeneracy and is therefore allowed in the spin degenerate bulk bands. In Equation 2.1, the photon drag effect photocurrent is

given by $j_\lambda = \sum_{\delta\mu\nu} T_{\lambda\delta\mu\nu} E_\mu E_\nu^*$. The fourth rank tensor $T_{\lambda\delta\mu\nu}$ indicates that there are no symmetry restrictions for the photon drag effect. [7]

The photon drag effect has been observed in semiconductors since as early as 1935. [7] The photon drag photocurrent density j, as measured on a semiconductor sample, may be modeled by the follow equation:

$$j = bK(\omega)I\frac{n_\omega}{cm*}e\tau_p \tag{2.5}$$

where coefficent b characterizes the fraction of the total momentum transferred from the incident photons to the electron system, $K(\omega)$ is the absorption coefficient, I is the light intensity, n_ω is the refractive index of the semiconductor, c is the speed of light, $m*$ is the effective mass of the carrier (the electron or hole), and τ_p is the the time during which the carrier retains the absorbed momentum. [7]

2.3 Polarization Dependent Photocurrent in the Topological Insulator

The surface currents observed in quantum wells are spin-polarized photocurrents because they occur in subbands of lifted spin degeneracy. Spin-polarized photocurrents also flow on the surface of the TI. The mechanism behind their excitation is shown in Figure 2-2

Figure 2-2 shows the 2-dimensional cross section of a TI surface Dirac cone. As explained in Chapter 1, on the surface of a 3D topological insulator, an electron's momentum and spin are locked perpendicular to each other. In the blue side of the Dirac cone, the slope is positive so the electrons propagate to the right. All these electrons propagating to the right necessarily have their spins aligned, pointing down. In the red side of the Dirac cone, the slope is negative so the electrons propagate to the left. These electrons are all spin up.

In Figure 2-2 a), the system is in equilibrium. Spin up electrons propagate in one direction, and spin down electrons propagate in the opposite direction. The red

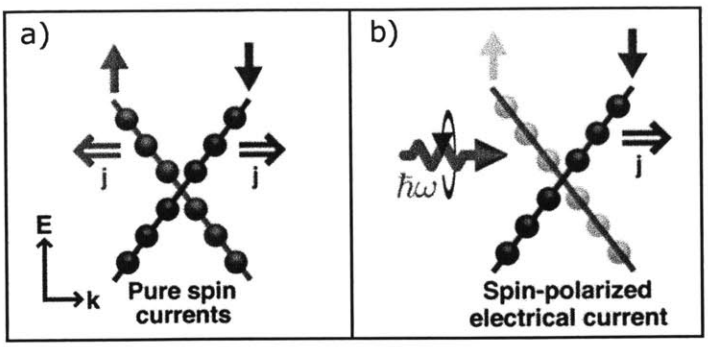

Figure 2-2: a) In equilibrium, pure spin current flows on the TI surface. b) When optically driven out of equilibrium, pure spin current is transformed into spin-polarized electrical current. Image source [16].

current traveling to the left cancels with the blue current traveling to the right, so there is no electrical current. However, there *is* a net flow of spin. This net flow of spin without net flow of charge is a pure spin current.

When the system is optically driven out of equilibrium, the situation shown in Figure 2-2 b) results. In Figure 2-2 b), circularly polarized light of energy $E = \hbar\omega$ is incident on the TI. Depending on the helicity of the light, the light will excite either the spin up electrons or the spin down electrons. Figure 2-2 b) shows the light exciting the spin up electrons which reside on the red side of the Dirac cone. The spin up electrons move up to excited states; this leaves the red half of the Dirac cone vacant and creates the $\vec{k}$-space asymmetry characteristic of the photogalvanic effect. The remaining electrons on the Dirac cone are all spin down and propagate to the right. The pure spin current has been transformed into a spin-polarized electrical current.

In Figure 2-3, we see how this same process occurs in the 3-dimensional Dirac cone, and how the spin-polarized photocurrent can be measured with an electrical device. Again, the electron spin and momentum are locked; the blue and pink arrows point in the direction of the electron spin. Circularly polarized light is incident on the TI, exciting the pink electrons but not the blue electrons. In Figure 2-3 a), the light propagates towards the right ($+x$ direction) and excites the electrons whose

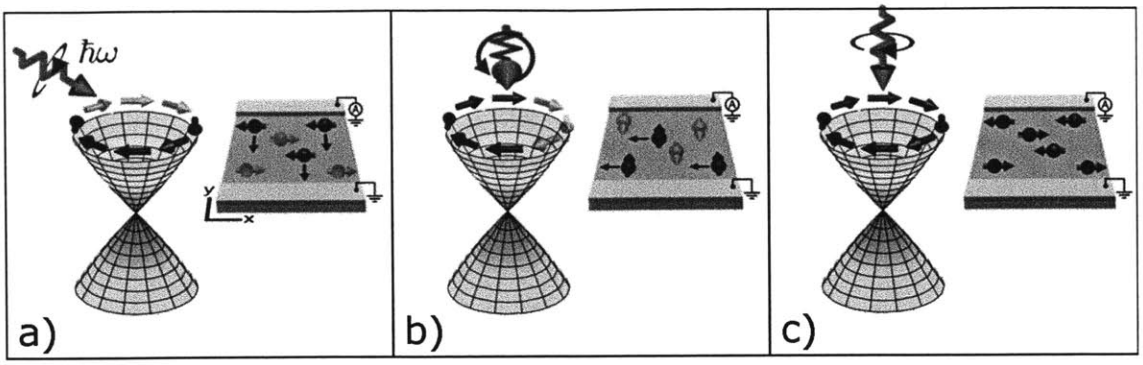

Figure 2-3: Spin-electrical current is excited on the 3-dimensional Dirac cone in $\vec{k}$-space. In real space, the current creates can be measured when it runs between 2 leads. Depending on the angle of incidence, the light will excite a photocurrent which can be measured (a), the light will excite a photocurrent which cannot be measured (b), or no photocurrent will be excited (c). Image source [16].

spins point in the $+x$ direction. Half of the Dirac cone is vacated by these pink electrons moving to excited states. The remaining blue electrons, whose spins point in the $-x$ direction, have momentum $\vec{k}$ directed out of the page (in the $-y$ direction). In real space, the electrical device has leads along the y-axis. The direction of the spin-polarized current (shown by the black arrows) is also along the y-axis, so the photocurrent is successfully measured by the electrical device.

In Figure 2-3 b), the light propagates in the $-y$ direction and excites the electrons whose spins point in the $-y$ direction. Again, half of the Dirac cone is vacated. The remaining blue electrons, whose spins point in the $+y$ direction, have momentum $\vec{k}$ in the $-x$ direction. Since the spin-polarized current flows along the x-axis and the leads are along the y-axis, this photocurrent is not successfully measured by the electrical device.

In Figure 2-3 c), the light propagates in a direction perpendicular to all the electron spins. There are no optical transitions and no photocurrent is generated.

In this thesis, we measured spin-polarized electrical currents on Bi_2Se_3 electrical devices. As mentioned in Chapter 1, in reality, residual bulk conductivity causes complications in attempts to study the 3D TI's surface states with transport experiments. However, with clever manipulation of lasers and optics, it is possible to distinguish

the TI's surface current from its bulk current.

In the experiments performed for this thesis, a radiation beam of changing polarization was shone on a Bi_2Se_3 device. The radiation beam was obliquely incident on the xz plane, inciting a photocurrent along the y-axis (as seen in Figure 2-3 a)). The light polarization was changed using a quarter wave plate which was rotated from angle $\alpha = 0°$ to $\alpha = 180°$. Over a single period, the polarization of the incident light was changed from p-polarized ($\alpha = 0°$) to left circularly polarized ($\alpha = 45°$), to p-polarized ($\alpha = 90°$), to right circularly polarized ($\alpha = 135°$), to p-polarized ($\alpha = 180°$). Analysis of how the TI's photocurrent changed with the changing light polarization revealed that there were 4 distinct contributions to the TI photocurrent. The photocurrent was modelled by the following 4 term equation:

$$j_y = Csin(2\alpha) + L_1 sin(4\alpha) + L_2 cos(4\alpha) + D \tag{2.6}$$

The first term on the right hand side of Equation 2.6 with coefficient C represents the photocurrent contribution from the circular photogalvanic effect, the second term with coefficent L_1 represents the contribution from the linear photogalvanic effect, the third term with coefficient L_2 represents the contribution from the photon drag effect, and the fourth term D represents a polarization-independent contribution. An example of photocurrent data fit to the model in Equation 2.6 is seen in Figure 2-4. [16]

The functional forms $sin(2\alpha)$, $sin(4\alpha)$, and $cos(4\alpha)$ in Equation 2.6 represent how the various contributions to the photocurrent vary with the changing light polarization as the quarter wave plate is rotated. The photocurrent C from the CPGE is modulated by the functional form $sin(2\alpha)$ because the the photocurrent is largest when the light is circularly polarized and 0 when the light is linearly polarized. It was determined through symmetry analysis that the photocurrent from the LPGE was modulated by the functional form $sin(4\alpha)$. The photocurrent from the photon drag effect is modulated by the functional form $cos(4\alpha)$, which indicates that the photocurrent is maximal when the light is p-polarized. This is expected since p-polarized

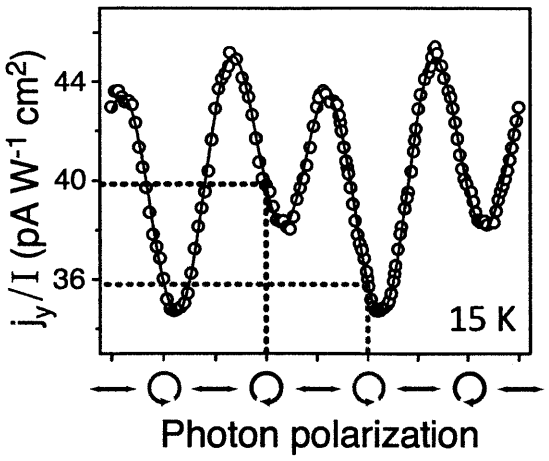

Figure 2-4: Photocurrent data fit to the model given in Equation 2.6. The image shows the photocurrent changing over 2 periods (the quarter wave plate rotates from $\alpha = 0°$ to $\alpha = 360°$). Image courtesy of James McIver.

light is the light absorbed most strongly by solids and the photon drag effect depends on linearly polarized light. [16] The fourth term D has no polarization dependence and represents a photocurrent offset from the bulk.

Chapter 3

Sample Growth and Device Fabrication

3.1 Sample Growth

The thin films of Bi_2Se_3 used in this thesis' photocurrent experiment were grown on sapphire substrates via molecular beam epitaxy (MBE), a process which grows crystals one layer at a time.

In MBE, a thin film material is heated to create an evaporated beam of particles, which is directed towards the substrate. The thin film forms by beam particles condensing onto the substrate surface. Because of the slow deposition rate ($\sim$ 1000 nm/hr), MBE must take place at high vacuum ($\sim 10^{-8}$ Pa) in order to maintain the sample's purity.

Previous experiments performed in the Gedik laboratory measured photocurrents on exfoliated flakes of Bi_2Se_3. Exfoliated flakes are fabricated by a process in which a piece of tape is used to pull layers off a large crystal. The crystal can be as thick as a centimeter before it is exfoliated. Although the photocurrent experiments on exfoliated Bi_2Se_3 were a success, fabricating Bi_2Se_3 devices on exfoliated flakes is very labor intensive. Furthermore, the exfoliated Bi_2Se_3 devices cannot be scaled up for technological applications.

This experiment used MBE thin films instead of exfoliated flakes since MBE thin

films are more promising for technology. MBE thin films are also highly ordered and have a well-defined orientation with respect to their crystalline substrates. This high order makes them preferable for experimental use.[19] The MBE thin films used in this experiment were grown at MIT by Dr. Ferhat Katmis.

3.1.1 Sapphire Substrates

In earlier attempts to measure photocurrent on MBE Bi_2Se_3 thin films, Bi_2Se_3 was grown on silicon substrates. These experiments were ultimately unsuccessful because large amounts of photocurrent were often inadvertently excited in the silicon, a semiconductor, thereby obscuring the desired Bi_2Se_3 photocurrent. It was determined that this overlap was due to the proximity of the silicon band gap (1.1 eV) to the Bi_2Se_3 band gap (0.3 eV). Therefore in the experiments performed for this thesis, sapphire, an insulator with a larger bandgap of 8.7 eV, was used instead of the silicon to avoid this problem.

The sapphire substrates used for this experiment were purchased by the Gedik laboratory from Shinkosha Co.. These substrates were cut into squares of area 1 cm $\times$ 1 cm, with 1 mm thickness. They were then diced into 4 squares of area .5 cm $\times$ .5 cm.

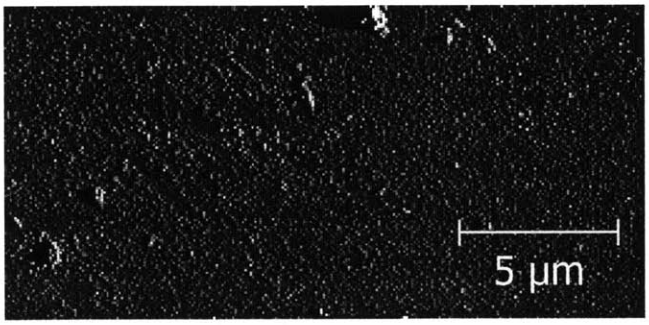

Figure 3-1: An image of the sapphire surface on a micron scale taken by atomic force microscopy.

At the start of the experiment, the smoothness of the sapphire's surface was characterized by atomic force microscopy (AFM). Figure 3-1 shows a micron-scale image

of the sapphire surface taken by AFM. Atomic force microscopy, also known scanning force microscopy (SFM), is a type of scanning microscopy which has resolution on the order of fractions of a nanometer. In AFM, a cantilever with a very sharp tip on its end is used to scan the surface of a sample. The sharp tip is typically made of silicon and has a radius of curvature on the order of nanometers. During the scanning, the tip is brought extremely close to the sample's surface, but without ever actually making contact. Because of this proximity, the tip feels atomic forces from the atoms of the sample's surface. The cantilever then experiences deflection according to Hooke's law due to these atomic forces. These deflections are measured using laser light and a photodiode, recording the surface image to very high resolution.

3.2 Device Fabrication

Experiments were performed on the Bi_2Se_3 thin films through electrical devices fabricated on their surface. The device fabrication involved photolithography, ion milling, and metal evaporation, processes which allow for accuracy on the nanometer scale. For these experiments, these processes were used to create devices of micron-scale size.

Photolithography, also known as optical lithography, is a process of microfabrication used to selectively remove parts of a thin film or a substrate. The technique can be used to etch or engrave thin films into precise shapes and sizes. Like photography, photolithography uses light to capture an image. In photolithography, exposure to light transfers a geometric pattern from a template, called a photomask, to a thin film coated with a light-senstive material called photoresist. When the photoresist is removed from the thin film via a chemical developer, it leaves the pattern from the photomask behind on the thin film.

The devices created for this experiment required 2 rounds of photolithography, one positve and one negative. Figure 3-2 provides a schematic of the device at each step of the fabrication process. In the first round, positive photolithography is used together with ion milling to remove all Bi_2Se_3 from the surface of the substrate,

except in the select places where devices are to be made. Each device only has a thin strip of Bi_2Se_3 at its center, as seen in Figure 3-2 a). The second round uses negative photolithography along with metal evaporation to deposit titanium and gold contacts on the Bi_2Se_3 strips. These contacts are shown in Figure 3-2 b). The final completed device, seen in Figure 3-2 c), consists of the superposition of the the Bi_2Se_3 layer (a) and the titanium and gold layer (b).

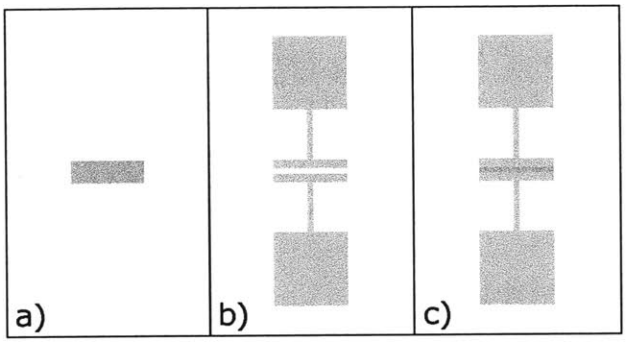

Figure 3-2: Schematic of a photocurrent device. a) The first round of photolithography and ion milling leaves a thin strip of Bi_2Se_3 on the sapphire substrate. b) The second round of photolithography and metal evaporation deposits titanium and gold contacts on the thin strip of Bi_2Se_3. c) A completed photocurrent device.

3.2.1 Procedure

The fabrication of the devices seen in Figure 3-3 involved 4 main steps detailed below: 1) positive photolithography 2) ion milling 3) negative photolithography and 4) deposition of titanium and gold. Steps 1), 3) and 4) were performed at MIT's Microsystems Technology Laboratories (MTL), and step 2) was performed at MIT's Francis Bitter Magnet Laboratory.

1. Positive photolithography is used to select the parts of the Bi_2Se_3 thin film which are *not* to be etched away by the ion miller in step 2). Before the process begins, the sample is first dehydrated or "baked" on an oven at 150° C, cleaning water and dust from the surface. Once the surface has been cleaned, a drop of positive photoresist, OCG825, is spun evenly across the sample's surface; the

spinning leaves a layer of photoresist around 1 μm thick. The photoresist-coated sample is then briefly "baked" once again before being exposed to ultraviolet light. This light exposure is done inside a mask aligner. In the mask aligner, the photomask, a glass sheet patterned with the device design, is placed between the sample and a UV lamp. When the UV lamp is turned on, the photomask therefore blocks certain parts of the sample from ultraviolet light exposure. This process effectively transfers the pattern from the photomask onto the sample. Post-exposure, the sample is "baked" once again before being washed in a chemical developer, OCG934. The developer washes away all the UV light-exposed photoresist, leaving most of the Bi_2Se_3 thin film surface unprotected. In the few areas where the photoresist was *not* exposed to the UV light and has *not* been washed away, the Bi_2Se_3 thin film retains a protective coating.

2. Next, an ion beam miller is used to remove the Bi_2Se_3 from all areas of the sample which are unprotected (i.e. *not* coated with photoresist). In this process, the sample is placed inside a vacuum chamber, where it is affixed to a rotating metal disk with vacuum grease. Argon gas is then allowed to flow into the chamber, and a high voltage is turned on across a filament at the chamber's ceiling. The high voltage creates a beam of argon ions which are then fired at the sample. During this process, the sample is rotated on the metal disk to ensure uniform ion bombardment across its surface. The beam of argon ions gradually etches away all the Bi_2Se_3 from all the surface's unprotected areas. When the milling is finished, the sample surface is bare sapphire with a few select areas of photoresist-coated Bi_2Se_3 thin film. The photoresist is then removed from the sample with acetone $(CH_3)_2CO$, a cleaning solvent, leaving behind the sapphire substrate with a few strips of the Bi_2Se_3 thin film. These strips of thin film form the Bi_2Se_3 portion of the photocurrent devices seen in Figure 3-2 a).

3. Negative photolithography proceeds similarly to positive photolithography (described above in step 1)) but with a negative photoresist, AZ5214, and corresponding developer, AZ422. A different photomask is also used to create the

contact pattern seen in Figure 3-2 b). For negative photolithography, the sample is exposed to the UV light twice, once with the photomask and once without. During the first exposure, the photomask must be aligned with the the sample so that the the contact pattern falls directly above the Bi_2Se_3 pattern, as seen in Figure 3-2 c). After the sample has been developed and rinsed, photoresist remains everywhere on its surface except in the select places where the contacts are to be deposited.

4. The final step of the device fabrication is titanium and gold deposition via a metal evaporator. As in step 2), this step takes place inside a vacuum chamber. The vacuum ensures that all extraneous vapors are removed from the chamber before the deposition begins. The sample is fastened to the vacuum chamber ceiling, and crucibles containing titanium and gold are loaded into the chamber's hearth. When the chamber is at a pressure nearing 2×10^{-5} Torr, a high voltage is turned on across a filament source. Electrons are emitted from the heated filament in a high energy beam which is directed at the crucible's center. The electron beam's intensity is increased until the metal in the crucible begins to evaporate. Because the chamber is at vaccum, the vapor metal particles rise directly to the chamber ceiling without any collisions or interference. Upon contact with the sample's surface, the particles condense back to the solid state, leaving a uniform coating. [3]

   The metal evaporation is performed twice to deposit first 10 nanometers of titanium, followed by 100 nanometers of gold onto the sample surface. Across the majority of the surface, the titanium and gold has evaporated onto the photoresist. But in the few photoresist-free areas, the metals have evaporated directly onto the actual sapphire substrate and Bi_2Se_3 thin film. When the metal evaporation is complete, the photoresist is washed away with acetone, removing most of the metal coating along with it. In the photoresist-free areas, the titanium and gold remain, forming the device's contacts. A completed device appears as in Figure 3-2 c).

3.2.2 Device functionality

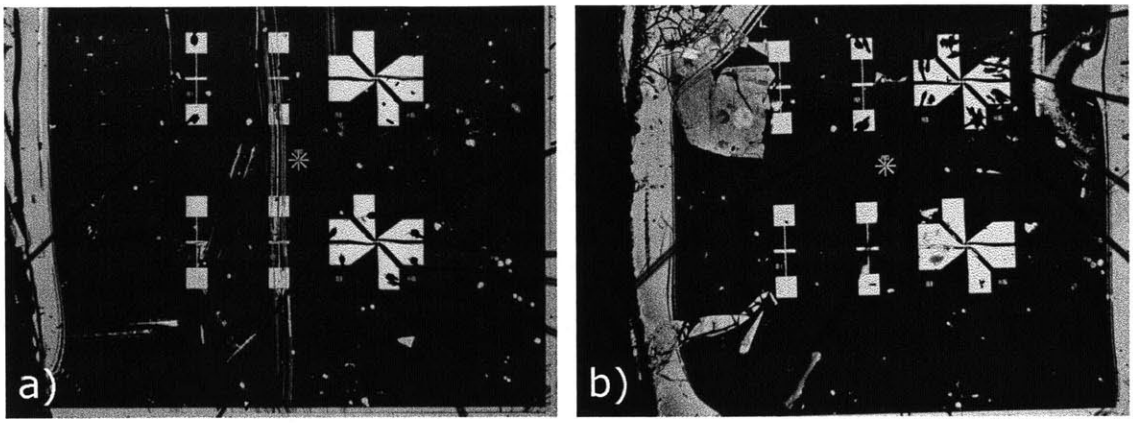

Figure 3-3: 2 completed chips: sapphire substrate with electronic devices made of Bi_2Se_3, titanium, and gold. Pictures were taken using a microscope, photo courtesy of Hadar Steinberg.

A single completed chip has 6 devices, as seen in the 2 examples chips shown in Figure 3-3. The 4 devices on the left side of the chip are the photocurrent devices used in this experiment. The photocurrent devices were designed to have long horizontal leads to allow for an experiment on the angle of incidence dependence. At large angles of incidence where the laser beam spot would become oblate, the long leads would still be able to absorb all the irradiating light. The remaining 2 devices on the right side of the chip are Hall bars used by our collaborators in Professor Pablo Jarillo-Herrero's group for experiments involving magnetism.

Once the device fabrication is finished, the completed chip is affixed to a chipholder with silver epoxy (a thermosetting polymer). The device's gold contacts are wirebonded onto the metal pads found on the chipholder surface. In the experiments performed for this thesis, circularly polarized light is shone on the thin strip of Bi_2Se_3 at the photocurrent device's center. The circularly polarized light incites a photocurrent in the Bi_2Se_3, which flows across the device and to the 2 conducting metal contacts. These wirebonded contacts conduct the photocurrent to the chipholder, which in turn connects to the electronic equipment used to measure the incited photocurrent. (This

electronic measurement is further detailed in Chapter 4.)

The chips displayed in Figure 3-3 each have one functioning photocurrent device and one functioning Hall bar. Errors in fabrication can result in shorted devices due to scratches (as seen in the right-side photocurrent devices in chip a)) or improper removal of titanium and gold (as seen in the upper left photocurrent device on chip b)).

Chapter 4

Experimental Setup

4.1 Experimental Geometry

The experimental geometry used for the photocurrent measurements taken in this experiment is diagrammed in Figures 4-1 and 4-3, where Figure 4-1 displays the optical setup and and Figure 4-3 displays the electronic wiring used to record the measurements.

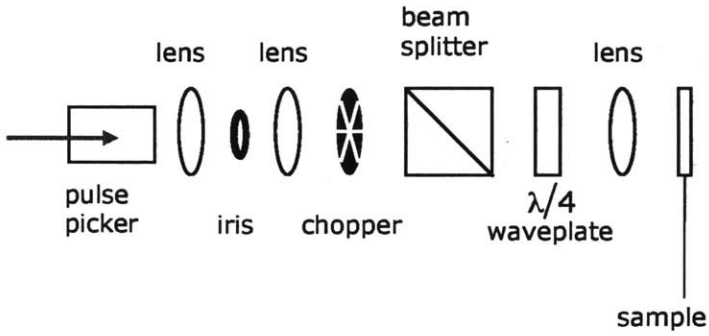

Figure 4-1: The optical setup used for the photocurrent measurements taken in this experiment.

In the optical setup, a fast pulse train generated by a Spectra-Physics laser was first directed into a pulse picker. A pulse picker is an electrically controlled optical gate which extracts a single pulse from a fast pulse train; here the pulse picker transmitted 1 pulse from every 50 pulses it absorbed. The laser power was measured using a power

meter and was varied between 600 μW and 30 mW.

From the pulse picker, the laser beam was then directed through a set of two lenses separated by an iris. The first lens had a focal length of 10 cm and the second had a focal length of 15 cm; the beam passed through these 2 lenses towards an optical chopper. The 15-blade chopper wheel was synchronized with electronic equipment to rotate at 1500 Hz. The laser beam was chopped through the rotating wheel before reaching the polarizing beam splitter. The beam splitter separated the *s*-polarized and *p*-polarized components of the laser light, sending the former to the left (or up in Figure 4-1) and the latter straight ahead (to the right in Figure 4-1). Now linearly polarized, the laser beam was sent though a quarter wave plate, an optical device which can change linearly polarized light to circularly polarized light and vice versa. One final lens, with focal length 10 cm, was then used to focus the now circularly polarized beam to a specific point of the chip.

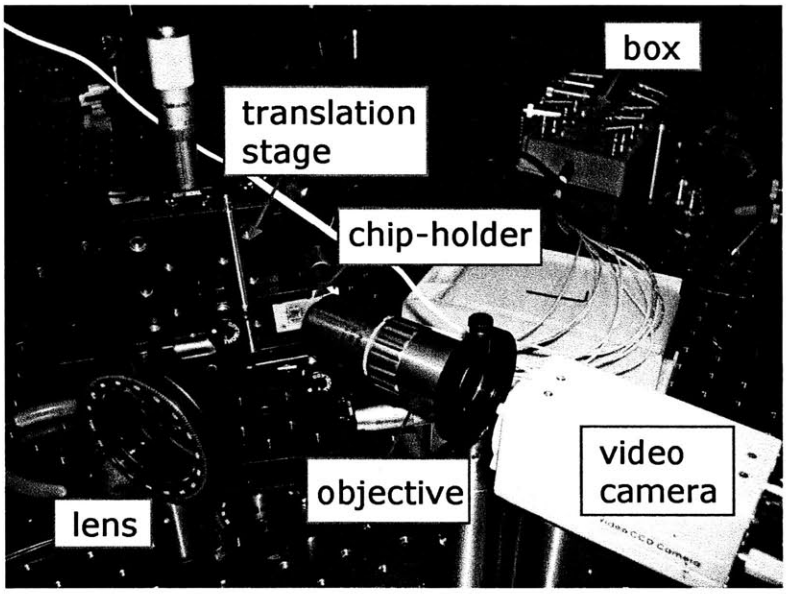

Figure 4-2: The translation stage, objective, and video camera used for the alignment of the radiation beam on the chip sample. The box contained electrical plugs which connected the chip sample to the electronic wiring in Figure 4-3.

The experiment required that the circularly polarized laser beam be incident on the Bi_2Se_3 portion of one of the chip's electrical devices to incite a photocurrent. Aligning the beam on these micron-scale devices would be exceedingly difficult to

do by the naked eye. Therefore, the alignment setup seen in Figure 4-2 was used. The setup consisted of an objective, a video camera, and a video monitor along with the focusing lens (with $f = 10cm$) mentioned in the previous paragraph. The chipholder was fastened onto a translation stage to further facilitate beam alignment. The translation stage allowed for movement along all three axes (x, y and z), as well as rotational motion. As an oblique angle of incidence was needed for the light to incite a spin photocurrent, the stage was rotated so that the laser beam hit the chip at an angle 45° to normal.

As mentioned in Chapter 3, the electrical devices fabricated on the chip's surface were wire-bonded to metal pads on the chipholder. Each chipholder had ten metal pads, which were connected to ten electrical plugs on a box as seen in Figure 4-2. This box was built specifically for this experiment by MIT undergraduate Steve Drapcho. The signals from the chip's devices were measured using the electrical plugs on this box, with the setup diagrammed in Figure 4-3. To measure the current across a photocurrent device, the device's two corresponding electrical plugs on the box were uncapped. One plug was connected to ground through the Sourcemeter, sending the signal through the second plug to an amplifier. The amplifer was set to a gain of 10^7. The amplified signal was then sent to a lock-in amplifier. A lock-in amplifer, also known as a phase-sensitive detector, is a type of amplifier which extracts a signal from a very noisy environment. In this experiment, the lock-in amplifier was synced with the optical chopper; it therefore bypassed the noise by only measuring the signal at the frequency of 1500 Hz. The signal from the lock-in amplifier was then recorded by a computer via a Labview program.

4.2 Quarter Wave Plate Calibration

The photocurrent measurements in this experiment were taken while the quarter wave ($\lambda/4$) plate was rotating, which varied the laser light continuously between different polarizations. In a quarter wave plate, a birefringent material (i.e. a material with 2 different indices of refraction) is used to create a phase shift between different

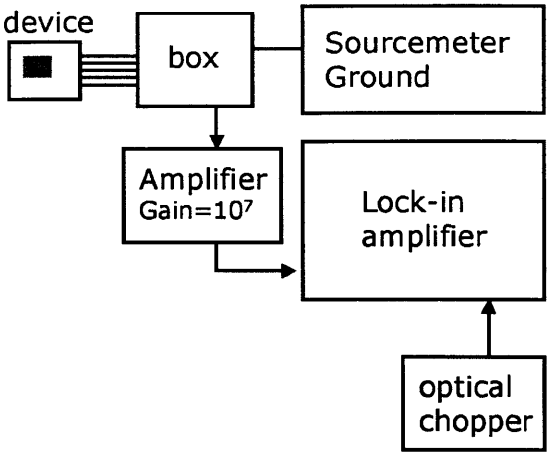

Figure 4-3: The electronic setup used for the photocurrent measurements taken in this experiment. The devices on the chip were connected to the electronic equipment through electrical plugs on the box.

components of light. Light which enters the material along the "fast axis" (also called the optic axis) passes through the wave plate more quickly than light which enters the material along the axis perpendicular to it, the "slow axis." The component of light traveling along the "slow" axis is retarded by 90° or a quarter wave, with respect to the component traveling along the "fast" axis. When the incident light makes an angle of 45° with the optic axis, then half the light travels along the "fast' axis and the other half along the "slow" axis. The emitted light is then circularly polarized and can excite the desired photocurrent

When paired with the polarized beam splitter used in the optical setup of our experiment (see Figure 4-1), a 180° rotation of the quarter wave plate changed the laser light from p-polarized, to left circularly polarized, to p-polarized, to right circularly polarized, and back again to p-polarized. The emitted light was p-polarized when the incident p-polarized beam was aligned with either the "fast" or "slow" axis; this was equivalent to angles of 0°, 90°, and 180° from the optic axis. When the incident p-polarized beam was incident at angle of 45° from the optic axis the emitted light was left circularly polarized, and at 135°, right circularly polarized.

At angles of the quarter wave plate where the light was p-polarized, minimal

spin photocurrent was excited. As the polarization was changed, the photocurrent increased, peaking at the angles with circularly polarized light. A full 360° rotation therefore gave a four peak trace, with 180° periodicity.

A single 360° rotation of the quarter wave plate required a few minutes. The wave plate rotation was controlled by a Newport Universal Motion Controller Drive which was accessed via the computer LabView program. This program was used to set the wave plate to rotate several hundred times over the course of a few hours during which photocurrent data was collected from the lock-in amplifier. The data was collected in such a way so that averaging over the traces could eliminate extraneous factors such as laser drift from the final data.

To calibrate the quarter wave plate before the data collection, 2 different calibrations were performed: a polarization intensity calibration and a laser intensity calibration. These two calibrations are further detailed below.

4.2.1 Polarization Intensity Calibration

The polarization intensity calibration was used to align the optic axis of the quarter wave plate with the *p*-polarized light from the beam splitter and also to confirm the correct formation of circularly polarized light at the appropriate angles.

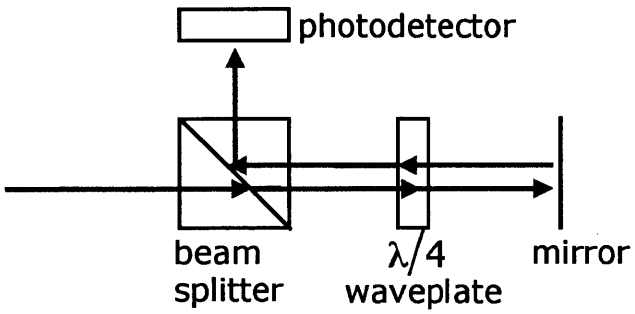

Figure 4-4: The experimental setup used to calibrate the quarter wave plate.

For this calibration, the setup seen in Figure 4-4 was used. The "chopped" laser beam was split into its *s* and *p* components by the beam splitter, as explained in the previous section. The *p*-polarized light passed through the quarter wave plate and

was reflected from a mirror, reversing the direction of light propagation. The reversed light beam was passed back through the quarter wave plate, returning to the beam splitter. At the beam splitter, the s-component of light was deflected towards the photodetector, while the p-component continued straight forward.

In the first part of the calibration, the quarter plate was stepped through different angles to find the direction of the optic axis. In this setup, when the p-polarized light forms an angle of 0° to the optic axis, no signal is observed in the photodetector. The quarter wave plate fails to retard any component of the light during both the forward and back portions of its path, so the p-polarized beam returns to the beam splitter unchanged and no s-polarized component is sent to the the photodetector. Finding this angle of minimum detected photodetector signal thus aligns the p-polarized light with the quarter wave plate's optic axis.

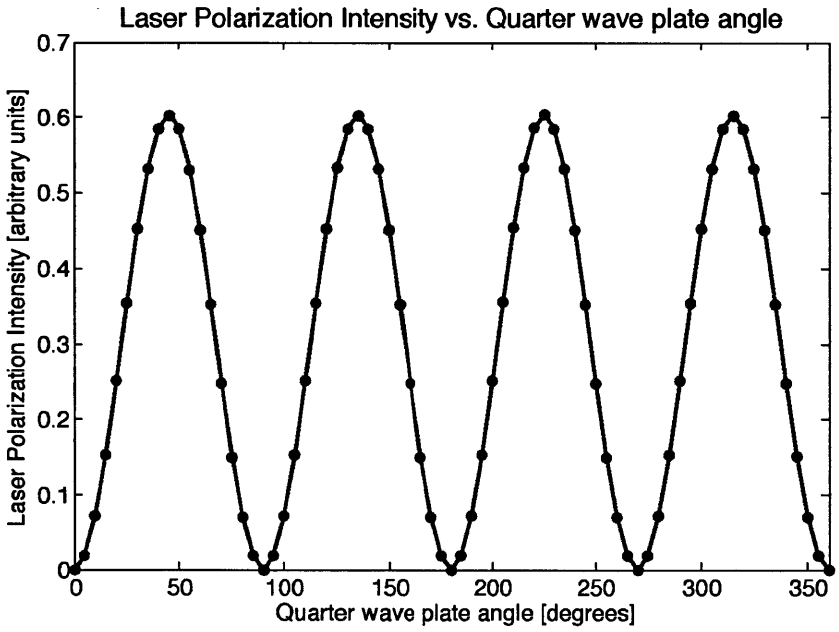

Figure 4-5: The trace from the polarization intentsity calibration confirmed that the quarter wave plate was functioning properly.

During the second part of the polarization intensity calibration, the quarter wave plate was set to continuously rotate, and a trace was taken of the photodetector signal. The trace from one of these calibrations is shown in Figure 4-5. The signal

is 0 whenever the p-polarized light is aligned with either the "fast" or "slow" axis. The 4 peaks correspond to the wave plate orientations generating circularly polarized light. For example, when the p-polarized light forms a 45° angle to the optic axis, the quarter wave plate transforms the linearly polarized light into left circularly polarized light. Upon reflection from the mirror, the light becomes *right* circularly polarized. The quarter wave plate changes this to s polarized light. The entire beam is now s-polarized and is entirely deflected by the beam splitter into the photodetector, creating a maximal signal.

In a perfectly cut quarter wave plate, the calibration trace should have the form $j \propto -Acos(4\alpha)$. The trace seen in Figure 4-5 fits well to this form, confirming that the quarter wave plate is functioning properly.

4.2.2 Laser Intensity Calibration

A second calibration, the laser intensity calibration was used to determine whether there was any intrinsic shape to the the laser beam signal. The setup for this calibration was essentially the same optical setup as that used for the photocurrent measurements, except with a photodetector in the place of the chip (see Figure 4-6).

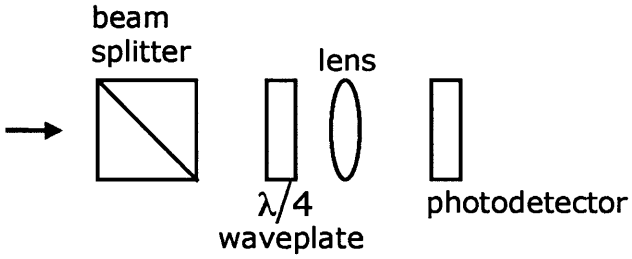

Figure 4-6: The experimental setup used to take the laser intensity calibration of the $\lambda/4$ wave plate.

A trace from this laser intensity calibration (shown in Figure 4-7) revealed that the laser beam signal did indeed have an intrinsic shape, but this signal was several orders of magnitude less than the signal that observed from the photocurrent on the

Bi_2Se_3. Therefore, even when the photocurrent data was corrected with the intensity calibration data, there was no significant alteration.

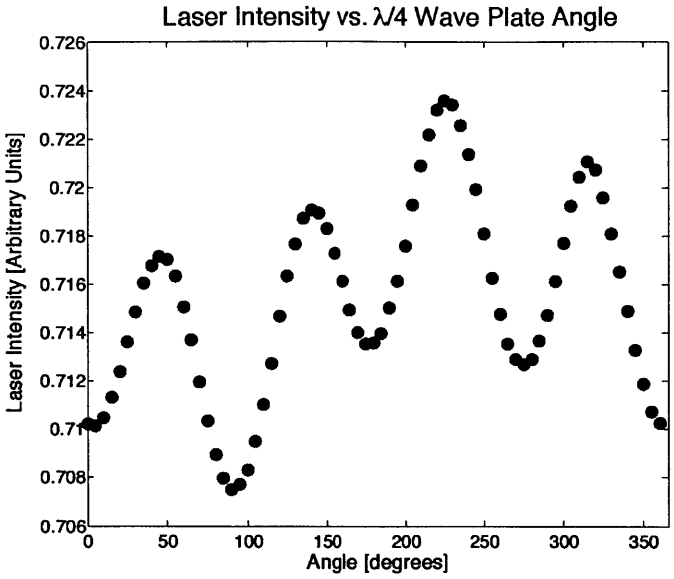

Figure 4-7: The trace from the intensity calibration revealed that the laser beam had an intrinsic shape, but the signal was small enough to be considered negligible.

Chapter 5

Experimental Results

5.1 Exfoliated Bi_2Se_3 photocurrent

The initial goal of our photocurrent experiments on MBE grown Bi_2Se_3 electrical devices was to replicate the results of a previous experiment in which photocurrent had been excited on exfoliated flakes of Bi_2Se_3. The exfoliated Bi_2Se_3 photocurrent experiments had been successfully performed by members of the Gedik laboratory, and the experimental results were published in the Nature Nanotechnology journal. [16] Figure 5-1 shows how the shape of the photocurrent signal measured on the exfoliated Bi_2Se_3 devices varied with changing laser light polarization.

The photocurrent signal seen in Figure 5-1 changes through 2 periods of changing photon polarization. This polarization was controlled by rotating a quarter wave plate from angle $\alpha = 0$ to $\alpha = 360°$. A single period involved rotating the quarter wave plate by 180°. During one period, the polarization changes from p-polarized at $\alpha = 0$, to left circularly polarized (σ^-) at $\alpha = 45°$, back to p-polarized at $\alpha = 90°$, to right circularly polarized (σ^-) at $\alpha = 135°$, and back again to p-polarized at $\alpha = 180°$. As discussed in Chapter 2, the shape of the photocurrent as it changes with the light polarization may be modeled by Equation 5.1:

$$j_y = Csin(2\alpha) + L_1 sin(4\alpha) + L_2 cos(4\alpha) + D \tag{5.1}$$

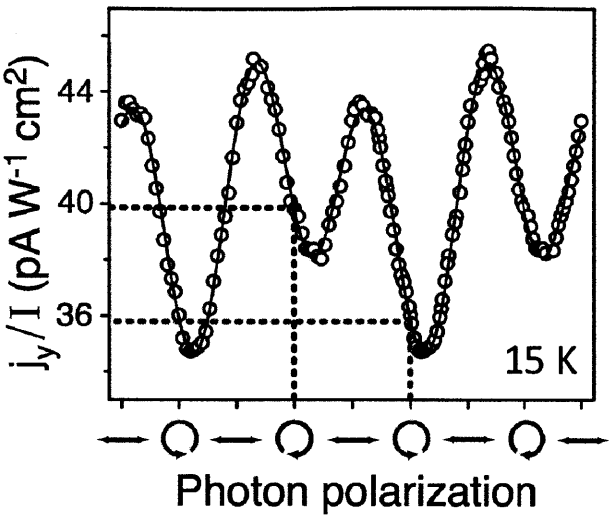

Figure 5-1: Helicity-dependent photocurrent measured on an exfoliated Bi_2Se_3 device. The data is fit to the model given in Equation 5.1. The photocurrent changes with the photon polarization over 2 periods. Image courtesy of James McIver.

5.2 MBE Bi_2Se_3 photocurrent

For this thesis, photocurrent was induced and measured on sapphire substrate MBE Bi_2Se_3 devices using similar methods to those used in the previous exfoliated Bi_2Se_3 experiment (for a more detailed explanation of these methods, see Chapter 4).

The results of the exfoliated Bi_2Se_3 experiment were successfully reproduced on our MBE Bi_2Se_3 devices. An example of the photocurrent measured on our MBE Bi_2Se_3 devices is shown in Figure 5-2. These results were fit to Equation 5.1. Like the exfoliated Bi_2Se_3 photocurrent shown in Figure 5-1, the MBE Bi_2Se_3 photocurrent repeats its shape through 2 periods of changing photon polarization.

The photocurrent shown in Figure 5-2 was taken at a laser power of 32 mW, with the laser spot size enlargened to illuminate the entire Bi_2Se_3 device at once. Figure 5-4 b) shows this defocused laser spot on the device.

Having confirmed that it was possible to induce and measure photocurrent on MBE thin films of Bi_2Se_3, we then attempted to repeat this measurement using a smaller spot size. A smaller spot size could be useful for technological applications and for an experiment on the angle of incidence dependence. As explained in Chapter

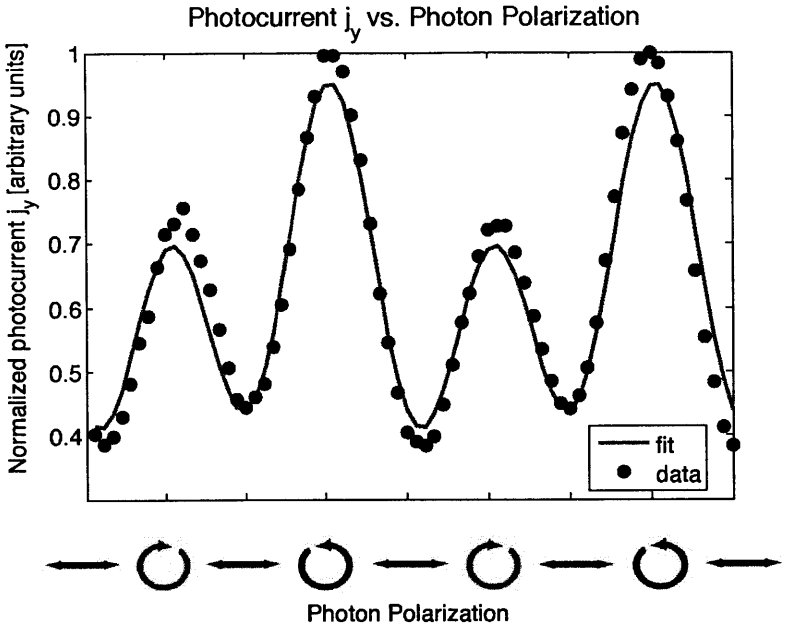

Figure 5-2: We successfully measured the desired photocurrent on our MBE grown Bi_2Se_3 devices. This photocurrent data is fit to the model given in Equation 5.1. The photocurrent changes with the photon polarization over 2 periods.

3, the photocurrent devices fabricated for this experiment were designed with long leads to allow for a focused laser beam to spread out on the device at large angles of incidence during such an experiment.

To obtain this smaller spot size, the laser power was turned down to 600 μW, and the laser beam was focused onto a smaller area of the Bi_2Se_3. The laser power was lowered to maintain the same light intensity on the device despite the decreased spot size of the beam. The photocurrent measurements were then re-taken with this focused beam. Surprisingly, the new photocurrent had an unexpected shape even after extensive averaging. As seen in the data presented in Figure 5-3, the data taken with the focused laser did not resemble the photocurrent data observed in Figures 5-1 or 5-2. The data also did not fit the mathematical model given in Equation 5.1. Even more disconcertingly, this new data failed to demonstrate the correct periodicity.

Figure 5-3 shows the photocurrent measured over 2 periods of changing photon polarization. We expect the photocurrent to display the same periodicity as the

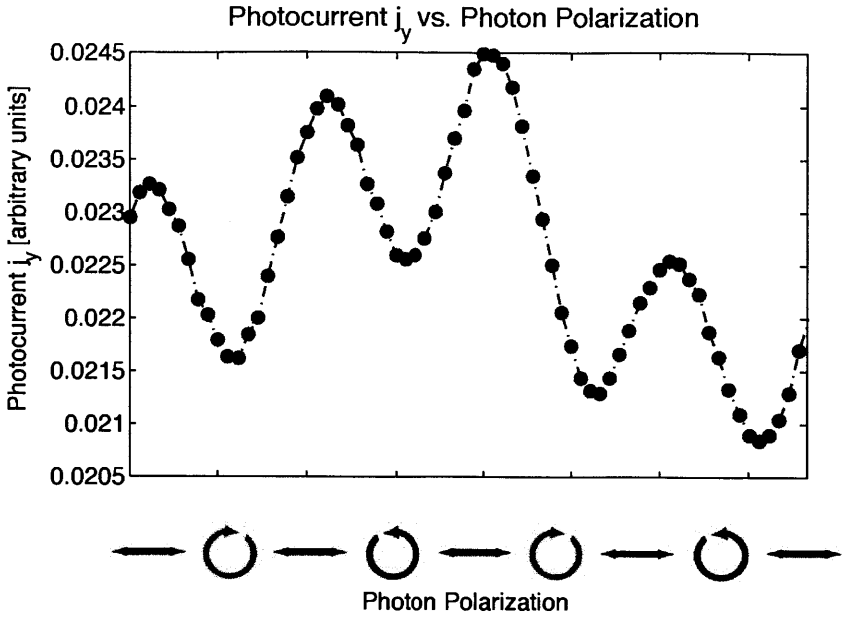

Figure 5-3: When the laser spot size was decreased, the photocurrent failed to fit the model given in Equation 5.1 and also did display the correct periodicity. The photon polarization goes through 2 periods, but the photocurrent does not reflect this.

photon polarization but it does not. Instead the photocurrent shape in the first period is entirely different from the shape in the second period.

The failure of the photocurrent data to reflect photon polarization periodicity appeared to be non-physical. It was initially suspected that the problem lay in our optics, specifically the quarter wave plate, the optic most responsible for controlling the laser beam light polarization. However, several calibrations of the quarter wave plate (detailed in Chapter 4) confirmed that the quarter wave plate was functioning properly. Replacing the quarter wave plate with a newer and cleaner quarter wave plate also failed to rectify the problem. This led us to conclude that the problem lay not in our optics or experimental setup but was due to some property of our Bi_2Se_3 devices.

Knowing that the expected photocurrent was successfully measured when the laser spot illuminated the entire device at once, we hypothesized that the focused laser beam was drifitng slightly on the Bi_2Se_3 device and inducing different photocurrents

at different areas on the device. Although ideally the focused laser beam should illuminate only one specific spot on the Bi_2Se_3 during the measurement process, in reality the laser pointing actually fluctuates with time. If multiple photocurrents were being induced on the same device during a single trace, the superposition of their signals might obscure the photocurrent's true shape.

5.3 Scanning laser light across the device leads

To test our hypothesis that fluctuations in the laser pointing were exciting various incongruous photocurrents on our MBE grown Bi_2Se_3 device, we took 6 photocurrent measurements with the laser beam focused at 6 different points along the electrical device's horizontal leads. These six points are diagrammed in Figure 5-4 a). We scanned the laser light across these 6 points by manually adjusting the translation stage by 2 μm between each point.

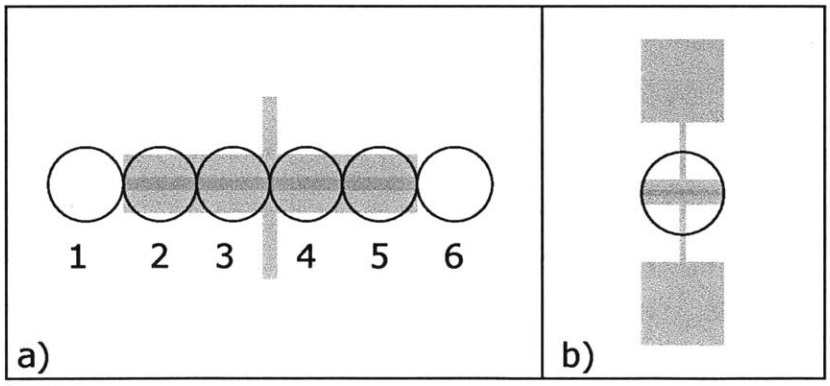

Figure 5-4: a) The laser beam was tightly focused on the Bi_2Se_3 device and scannned across 6 points along the horizontal leads. b) The photocurrent data shown in Figure 5-2 which displays the correct periodicity was taken with the laser beam defocused. The spot size was enlargened to illuminate the entire Bi_2Se_3 device evenly.

When the laser beam was focused at positions (1) and (6) in Figure 5-4 a), no photocurrent was observed and only noise was measured. A graph of the noise generated at position (6) is shown in Figure 5-5. This result successfully confirmed that

no photocurrent was being generated in the sapphire substrate, which was expected since sapphire is an insulator with bandgap 8.7 eV.

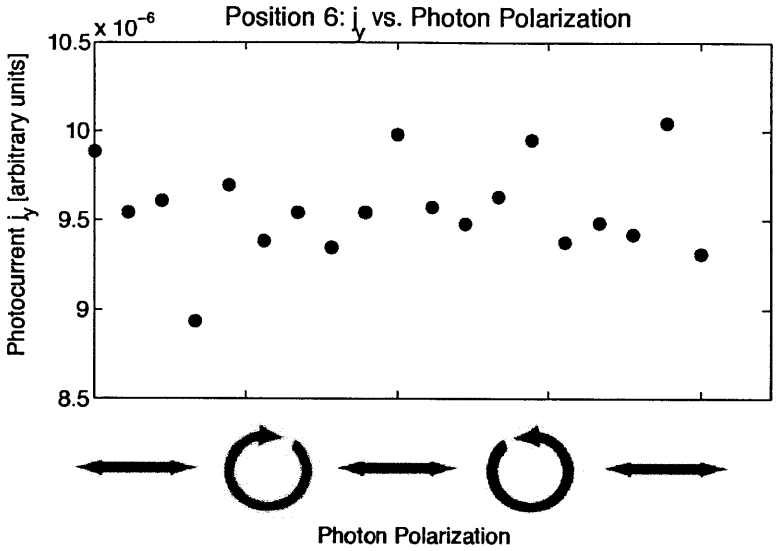

Figure 5-5: Position (6): when the laser beam was focused on the sapphire substrate instead of the Bi_2Se_3, no photocurrent was observed. This noise confirmed that the sapphire was insulating. Noise was similarly observed with the laser focused at position (1). The photon polarization goes through 1 period.

When the laser beam was focused on the Bi_2Se_3 device at positions (2) through (5), the photocurrent (like the photocurrent shown in Figure 5-3) did not display the correct periodicity. As shown in Figure 5-6, the shape of the photocurrent signal was different at each of the 4 points.

When the laser beam spot was returned to 1 of the 4 positions along the horizontal leads, the photocurrent generated at that position had a replicable shape, as seen in Figure 5-7. Figure 5-7 shows that the photocurrent measured at Position 3 was replicable over 2 traces taken during 2 different scans of the laser beam across the device leads.

The results of Figures 5-6 and 5-7 supported our hypothesis that different competing photocurrents were being excited by our focused laser beam. Fluctuations in the laser pointing over time excited these different photocurrents, preventing observation of a single photocurrent with a periodicity matching that of the photon polarization.

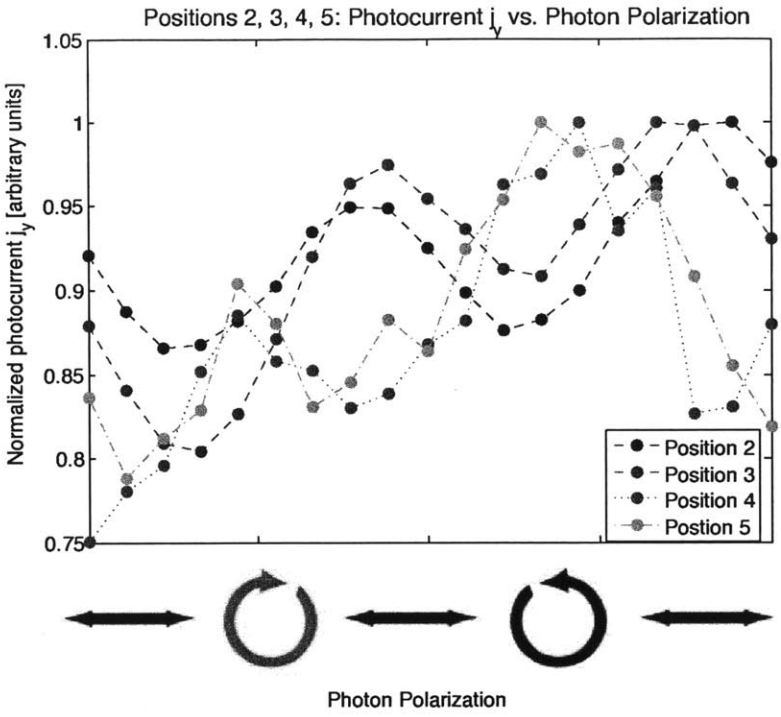

Figure 5-6: The photocurrent shape was different when the laser beam was focused at 4 different points along the Bi_2Se_3 device's horizontal leads. The photon polarization goes through 1 period.

This problem had been bypassed when the laser spot was large because laser pointing fluctuations did not noticeably change the device illumination in that case.

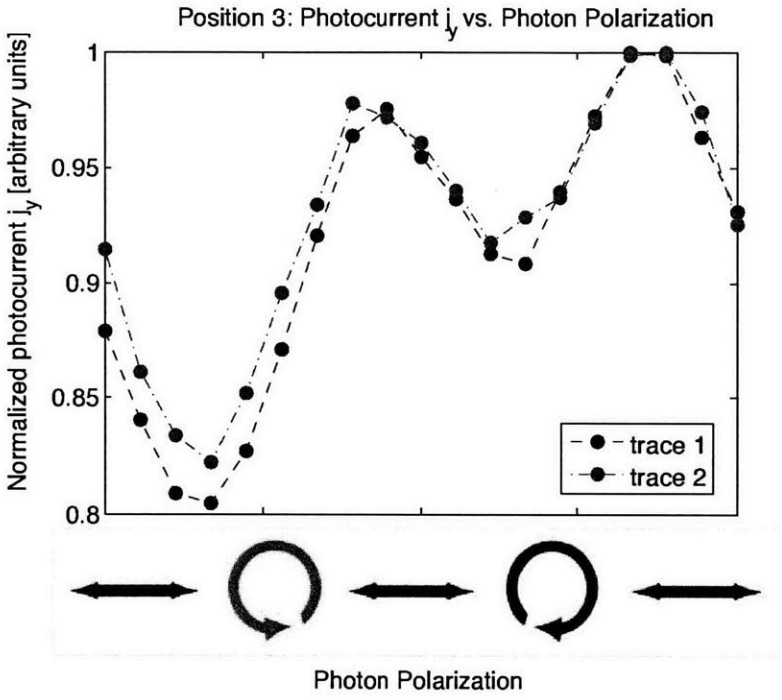

Figure 5-7: Position (3): the photocurrent shape with the laser beam focused at a specific point along the Bi_2Se_3 device's horizontal leads was replicable. The photon polarization goes through 1 period.

Chapter 6

Conclusions

In conclusion, we were able to successfully excite and measure polarization dependent photocurrent on MBE thin films of Bi_2Se_3 grown on sapphire substrate. The measured photocurrent agreed with the results of an earlier photocurrent experiment which used exfoliated flakes of Bi_2Se_3. We successfully fit our photocurrent data to a model equation, showing that there were photocurrent contributions from the circular photogalvanic effect, linear photogalvanic effect, and photon drag effect.

We were unable to reproduce our photocurrent results when we focused our laser beam onto a smaller area. The expected polarization dependent photocurrent could be measured only when the spot size was large enough to illuminate the entire Bi_2Se_3 device evenly. When a smaller spot was focused on only a part of the Bi_2Se_3 device, we measured seemingly non-physical photocurrent. The smaller spot size photocurrent could not be fit to our model equation and did not reflect the periodicity of the incident photon polarization.

It was hypothesized that the seemingly non-physical photocurrent was due to the excitation of multiple photocurrents at different points of the device. The laser pointing fluctuated slightly with time, and therefore when the laser was tightly focused it would illuminate different areas of the device during a single trace. The sum of the photocurrents excited in this manner did not yield the true photocurrent shape.

This hypothesis was supported by the results of an experiment where we scanned the laser beam horizontally across the device's leads. At each of the 4 points along

the device, the photocurrent shape was replicable but different from the shape at the other points. The observation of these different photocurrents led us to conclude that there was indeed something inhomogeneous about our device.

It was suggested that this device inhomogeneity was due to the polycrystalline nature of our MBE grown Bi_2Se_3 devices. In previous experiments, photocurrent was measured across exfoliated Bi_2Se_3. In these exfoliated flakes, an electrical device was fabricated across a single crystal of Bi_2Se_3. In our experiment, the electrical devices were fabricated to span across multiple crystals on the Bi_2Se_3 surface. It was therefore possible that when our laser beam was focused at different points of the electrical device, multiple photocurrents propagating in different directions were excited in these crystals. However, we are unsure of the validity of this explanation. The crystals of our MBE thin film Bi_2Se_3 are very small, so the different photocurrents in these crystals would likely average out. Currently, the underlying reason behind the device inhomogeneity remains under investigation.

Bibliography

[1] B. Andrei Bernevig. Quantum spin Hall effect and topological phase transition in HgTe quantum wells. *Science*, 314:1757–1761, December 2006.

[2] B. Andrei Bernevig and Shou-Cheng Zhang. Quantum spin Hall effect. *Physical Review Letters*, 96(106802), March 2006.

[3] Kurt Broderick. *E-beam Standard Operating Procedure.*

[4] Jeff Brumfiel. Topological insulators: Star material. *Nature*, 466:310–311, July 2010.

[5] Liang Fu and C.L. Kane. Topological insulators with inversion symmetry. *Physical Review Letters*, 76(043502), July 2007.

[6] Liang Fu, C.L. Kane, and E.J. Mele. Topological insulators in three dimensions. *Physical Review Letters*, 98(106803), March 2007.

[7] S. D. Ganichev and W. Prettl. *Intense Terahertz Excitation of Semiconductors.* Oxford Scholarship Online, September 2007.

[8] S.D. Ganichev and W. Prettl. Spin photocurrents in quantum wells. *Journal of Physics: Condensed Matter*, 15:R935–R938, May 2009.

[9] David J. Griffiths. *Introduction to Quantum Mechanics.* Pearson Education, Inc., second edition, 2005.

[10] M. Z. Hasan and C. L. Kane. Colloquium: Topological insulators. *Reviews of Modern Physics*, 82, November 2010.

[11] D. Hsieh, D. Qian, L. Wray, Y. Xia, Y.S. Hor, R.J. Cava, and M.Z. Hasan. A topological Dirac insulator in a quantum spin Hall phase. *Nature*, 452, April 2008.

[12] D. Hsieh, Y. Xia, L. Wray, D. Qian, A. Pal, J.H. Dil, J. Osterwalder, F.Meier, G. Bihlmayer, C.L. Kane, Y.S. Hor, R.J. Cava, and M.Z. Hasan. Observation of unconventional quantum spin textures in topological insulators. *Science*, 323, February 2009.

[13] David Hsieh. Spin-resolved spectroscopic studies of topologicall ordered materials, June 2009.

[14] Charles L. Kane. An insulator with a twist. *Nature Physics*, 4(5):348–349, May 2008.

[15] C.L. Kane and E.J. Mele. Z_2 topological order and the quantum spin Hall effect. *Physical Review Letters*, 95(146802), September 2005.

[16] J.W. McIver, D. Hsieh, H. Steinberg, P. Jarillo-Herrero, and N. Gedik. Control over topological insulator photocurrents with light polarization. *Nature Nanotechnology*, 7:96–100, 2012.

[17] J.E. Moore and J. Orenstein. Confinement-induced berry phase and helicity-dependent photocurrents. *Physical Review Letters*, 105(026805), July 2010.

[18] Joel Moore and Charles Kane. Topological insulators. *Physics World*, February 2011.

[19] Joel E. Moore. The birth of topological insulators. *Nature*, 464, March 2010.

[20] Rahul Roy. Z_2 classification of quantum spin Hall systems: an approach using time-reversal invariance. *Physical Review B.*, 27(195321), May 2009.